Properties of a diffuse interface model based on a porous medium theory for solid–liquid dissolution problems

Haishan Luo · Michel Quintard · Gérald Debenest · Farid Laouafa

Abstract In this paper, a local non-equilibrium diffuse interface model is introduced for describing solid–liquid dissolution problems. The model is developed based on the analysis of Golfier et al. (J Fluid Mech 457:213–254, 2002) upon the dissolution of a porous domain, with the additional requirement that density variations with the mass fraction are taken into account. The control equations are generated by the upscaling of the balance equations for a solid–liquid dissolution using a volume averaging theory. This results into a *diffuse interface model* (DIM) that does not require an explicit treatment of the dissolving interface, e.g., the use of arbitrary Lagrangian–Eulerian (ALE) methods, for instance. Test cases were performed to study the features and influences of the effective coefficients inside the DIM. In particular, an optimum expression for the solid–liquid exchange coefficient is obtained from a comparison with the referenced solution by ALE simulations. Finally, a Ra–Pe diagram illustrates the interaction of natural convection and forced convection in the dissolution problem.

Keywords Diffuse interface model · Porous medium theory · Numerical simulation

Mathematics Subject Classifications (2010) 76V05 · 76S05

H. Luo (✉) · M. Quintard · G. Debenest
Institut de Mécanique des Fluides de Toulouse,
Université de Toulouse; INPT, UPS,
Allée Camille Soula, 31400 Toulouse, France
e-mail: hshluo@gmail.com

M. Quintard
e-mail: Michel.Quintard@imft.fr

G. Debenest
e-mail: Gerald.Debenest@imft.fr

H. Luo · M. Quintard
CNRS, IMFT, 31400 Toulouse, France

H. Luo · F. Laouafa
Institut National de l'Environnement Industriel
et des Risques, Parc techncologique ALATA BP2,
60550 Verneuil-en-Halatte, France
e-mail: Farid.Laouafa@ineris.fr

Nomenclature

$A_{\beta\sigma}$	Surface between the β-phase and the σ-phase (square meters)
$D_{A\beta}$	Molecular mass diffusion coefficient (square meters per second)
g	Gravity (meters per square second)
K	Permeability (square meters)
$K_{\beta\sigma}$	Mass exchange between the β-phase and the σ-phase
$\boldsymbol{n}_{\beta\sigma}$	Normal vector to the β–σ surface
p	Pressure (pascal)
P	Averaged pressure (pascal)
V	Volume (cubic meters)
$\boldsymbol{v}_{\beta}$	β-Phase velocity (meters per second)
$\boldsymbol{v}_{\sigma}$	σ-Phase velocity (meters per second)
$\boldsymbol{v}_{A\beta}$	Velocity of species A in the β-phase (meters per second)
$\boldsymbol{v}_{B\beta}$	Velocity of species B in the β-phase (meters per second)
$\boldsymbol{V}_{\beta}$	β-Phase averaged velocity (meters per second)
$\boldsymbol{w}$	Interface recession velocity (meters per second)
α β-σ	Phase mass exchange coefficient (per second)

ε_β	β-Phase volume fraction
ρ	Density (kilograms per cubic meter)
$\tilde{\mu}$	Chemical potential (joules per mole)
μ	Dynamic viscosity (pascal second)
$\omega_{A\beta}$	Mass fraction of species A in the β-phase
$\Omega_{A\beta}$	Averaged mass fraction of species A in the β-phase

1 Introduction

Dissolution of solid matter or porous media is a typical problem widely encountered in many industrial fields, for instance, to mention a few applications, alloy melting, corrosion of carbonate rocks, acid injection into petroleum reservoirs, ablation of composite layers in rocket nozzles, etc... In the case concerned by this paper, dissolution of soluble rocks, e.g., salt mines, may lead to the expansion and collapse of the underground cavity, as illustrated in Fig. 1, which is a potential environmental risk. Numerical modeling of the evolving cavity is a method of choice for any safety analysis. Several numerical works were concerned by the dissolution of porous media, such as those done by [15, 52, 53]. While the model studied in this paper is directly linked to these approaches and, therefore, can handle true fluid/porous media dissolution problems, we are interested in applications for which the flow in the "solid" domain is close to zero, either because of very slow permeability or because the permeability itself is zero. In these situations, the solid and liquid bulks are connected directly by an interface at any scales, which, in principle, may preclude the direct utilization of porous media models. Instead, it should be regarded as a type of moving interface problem, and many direct techniques have been designed to handle such cases, such as the arbitrary Lagrangian–Eulerian (ALE) technique used as a "reference" in this paper. However, we show in our work, on the basis of a quantitative comparison with "reference" computations, that porous media

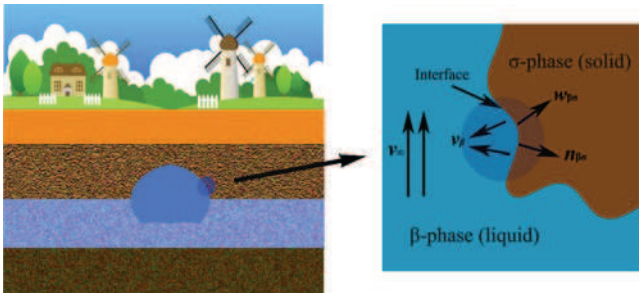

Fig. 1 Solid–liquid dissolution caused by groundwater

local non-equilibrium theories can indeed be used to deal with such problems.

For sake of simplicity, we consider the case of a binary system, i.e., the chemical solute constituting the solid is dissolved by a "solvent" (mainly water in most practical applications). Dissolution is controlled in this case by thermodynamic equilibrium at the interface, i.e., equality of the chemical potentials. This equality translates, for such a two-component system, into a simple Dirichlet condition for the concentration at the solid–liquid interface. An alternative choice for the boundary condition is to apply a reactive model, i.e., the mass flux between solid and fluid at the interface is determined by a reaction term. In most practical cases, e.g., salt mines, the reaction rate is very fast so that the reactive model approaches to the former boundary model, or the dissolution model based on equilibrium conditions is correct. Without loss of generality, we only consider very fast chemical reactions in this paper, or purely thermodynamic equilibrium problems. When applying this boundary condition to the mass transport equations that control the dissolution process, the solution of these PDEs will lead to a recession of the interface.

From a numerical point of view, there are two classes of approaches to characterize the moving interface: sharp interface methods and diffuse interface methods. Sharp interface methods can be further divided into two categories: front tracking and front capturing. Several front-tracking methods utilize a fixed grid with moving marker particles to track the fronts, such as [13, 23, 35, 39]. Some front tracking methods adopt a separate grid, for example, the famous ALE method handles the computation in both an absolute frame and a relative frame, the movement of the mesh being taken explicitly in the Eulerian frame [12, 22]. Also, various explicit treatments of the interface movement have been developed in the framework of finite discretization, e.g., finite volume formulation [44], random walk methods [4], etc... Recently, [51] developed an interface marker reconstruction method combined with a hybrid lattice-Boltzmann/finite-difference scheme [17]. These works have shown impressive simulation results. However, the major drawback of direct front tracking is the complexity. Special care has to be taken to topological changes, e.g., the algorithm of the redistribution of the interface markers is complicated. Further, the methods may have a poor behavior in the case of non-differentiable surfaces, for example, sharp angles. Compared to the explicit expression of the interface in the front-tracking methods, the interface is regarded implicitly in the front-capturing methods. The two most popular front-capturing methods are

volume of fluid (VOF) [16, 30] and level set [26, 34]. VOF method uses a color function to represent the phase volume fraction, which is subject to numerical diffusion. Therefore, reconstruction of the interface must be implemented. VOF methods have been associated with reconstruction algorithms that can handle streaks or peaks in interfacial gridblocks (development of specific piecewise linear interface calculation method like in [20]). For the level-set method, the interface is generally represented by the zero contour of a signed distance function (level-set function). The movement of the interface is governed by an advective equation for the level-set function, which is also affected by numerical diffusion. A reinitialization process is required in order to maintain the level-set function as a signed distance function. However, level-set method is often reported as nonconservative. To overcome this weakness, [24] proposed to use a Heaviside function to take the place of signed distance function as a level-set function. Better conservation is observed by this improvement. In fact, one can already find an initial trace of diffuse interface methods inside the VOF and recent level-set methods, as they have utilized the concept of phase field. However, the two methods still belong to sharp-front methods because the reconstruction or reinitialization of the interface can not be avoided. As the other big class of moving interface methods, the diffuse interface methods (DIM) consider the interface to be a diffuse layer where some quantities (especially a scalar field that plays the role of the phase indicator) vary rapidly but continuously [1, 3, 5, 19, 50]. This kind of opinion can be even dated up to two centuries ago, when Van der Waals [43] proposed that the physical interface should be continuous as a result of surface tension. The advantage of DIM compared to the sharp-front methods is that it does not need any special operation upon the interface during the computation. Global control equations can be applied to the whole domain without phase distinctions, thus greatly improving the facility of coding and computation. In the past three decades, the DIM has been extensively developed for many moving-interface problems, e.g., flows in near-critical fluids [25], capillary waves [40], moving contact lines [33], droplet and nucleation [9], dendritic growth and solidification [8, 32, 45], adsorption/desorption of material [37], metal alloys melting [18, 38], micro-scale solute precipitation and dissolution [42, 49], to list a few. These DIM works are generally based on the Cahn–Hilliard model [7], which is based on a free energy involving second gradient terms to "diffuse" the interfaces. Using real fluid characteristic leads to a physical interface, which is very thin in the case of solid–liquid dissolution. Very huge grid numbers are thus required to capture the narrow interface. In addition, the Cahn–Hilliard model contains fourth-order derivatives, which requires high-order numerical schemes. Adaptive mesh refinement is often applied to resolve around the interface to avoid the intolerable resource consuming, such as shown in [37]. Anyhow, the corresponding computations are often limited to a very small spatial scale, which could not meet the need for larger-scale simulations, such as those discussed in this paper. In addition, Cahn–Hilliard models in the case of multi-component problems pose several formulation problems with strong density variations, which are difficult to overcome. These difficulties motivated our study based on a completely different approach.

We take notice of the work of [15], who used a Darcy-scale local non-equilibrium model to study the dissolution regimes and wormhole development of porous media under different Pe and Da numbers (there is also a reminiscence of a local non-equilibrium theory in the case of solidification involving mushy zones [6, 31]). It is found that the porosity front becomes sharp when the mass exchange coefficient (which also can be understood as a Darcy-scale reaction rate that should not be confused with the pore-scale reaction rate) becomes large. The dissolution zone (if hydrodynamically stable) reaches rapidly a steady-state thickness, which may be controlled through the model parameters, in particular the mass exchange coefficient. In the limit of infinite mass exchange coefficient (in numerical practice: large enough), one recovers the local equilibrium dissolution front, i.e., a liquid–solid interface. This phenomenon is also observed by [51–53]. In particular, they all found that the dissolution front can become unstable under certain conditions, e.g., large Da numbers [15, 51], or based on the critical Zhao number proposed in [52, 53]. Regardless of these instability mechanisms, the main point of these various studies is that, with the increase of the mass exchange coefficient, the dissolution mechanism will be limited by the mass transport toward the interface region. That is to say, the front moving velocity will not depend on the mass exchange coefficient beyond a certain critical value. Mathematically speaking, a finite mass exchange coefficient will not lead to an extremely sharp porosity profile. How can we use such porous media theories for problems involving solid–liquid interfaces? In fact, we can consider the solid–liquid interface as a porous medium region where the porosity varies from 0 to 1. The mass exchange coefficient in the interface region can be artificially increased in order to sharpen the interface, while there is no need for an infinite value as discussed before. We only need to find a critical value to maintain a sufficiently sharp diffuse

interface, compatible with the physics we want to reproduce (for instance compatible with the boundary layers developing near the dissolving interface, as will be discussed later). As a result, a moderate mesh size can be used without generating significant inaccuracy. Based on this discussion, we follow the work of [15], then develop a DIM for solid–liquid dissolution problems. This model is obtained from a volume averaging technique. The resulting equations feature two mass balance equations for the liquid involving an effective diffusion coefficient, D^*, and a mass exchange term, α, both terms being a function of the porosity, ε_β. The momentum equation that approaches the initial physics is a Darcy–Brinkman equation, which degenerates to Stokes equations when in the free fluid and Darcy's law, with a permeability $K(\varepsilon_\beta)$, when in the diffuse interface region. Mathematically speaking, the interface in this model tends to be infinitively thin when the α coefficient tends to infinity. The thickness of the interface increases when α decreases. Therefore, α may be adjusted to reproduce approximately the interface at the desired accuracy. A very large α must not be used to avoid numerical resolution problems associated to very thin interfaces. In this paper, the α, D^*, and K are obtained by solving "closure problems" with a unit cell abstracted from a plane flow. Since no real porous medium is present, meaningful modifications could be made to optimize their expressions. Several choices will be discussed in this paper. In addition, the density variation is added in the current model not only because of mass conservation accuracy reasons but also because of the Rayleigh–Bénard effects aroused by gravity [21, 47, 48], which may have a great impact on the evolution of the dissolution interfaces.

A one-dimensional analytical solution giving the boundary velocity is obtained to verify the DIM by comparison with the one obtained from the original sharp interface model. We would like to mention here that an alternative approach to prove the coincide of the original model and the phase-field model is based on the utilization of asymptotic techniques [42]. Following this mathematical analysis, an upscaled model for crystal dissolution and precipitation was derived, which is quite similar to the one proposed in this paper[41]. The convergence analysis, though, does not include the effect of advection, which is an important part of the investigation presented in this paper. The DIM model properties and performances will be analyzed on a classical test case involving the dissolution of a plane-flow structure. Finally, we will use the validated model to understand the impact of density variations on a tube dissolution problem. Indeed, flow and geometry evolutions will be controlled by the competition between advection and diffusion (as measured by a Péclet number, Pe) and the possible effect of hydrodynamic instabilities (natural convection, depending on the value of a Rayleigh number, Ra). Our numerical results show that diverse configurations may be obtained: the appearance of a thin boundary layer when Pe increases and the appearance of hydrodynamic instabilities (salt fingers) at high Ra numbers. This latter aspect is particularly important as it tends to complicate the geometric structure of the dissolving interface (dissymmetry, roughnesses, ...).

In the next section, the diffuse interface model is deduced with the help of a volume averaging theory. In the third section, several examples are implemented to study the influence of the chosen effective coefficients. Finally, to illustrate the potential of the proposed model, a series of computations allow to plot a Pe–Ra diagram showing the various flow and geometry patterns obtained under different conditions.

2 Dissolution model

Figure 1 illustrates the exact interface for a solid–liquid dissolution problem. In the case of the binary system under investigation, the species concentration equals to an equilibrium value at the interface. We introduce a phase indicator, ε_β, that has a unit value in the liquid and zero in the solid in the original dissolution model, as shown in Fig. 2. Alternatively, for a diffuse interface method, the sudden jump of the variables will be replaced by a continuous distribution. A diffuse interface model may be obtained from different points of view, for instance on the basis of heuristic arguments. Because this brings some understanding on the physical soundness of the model, we adopt here the idea that this model is an application of porous media non-equilibrium theories. In this paper, the DIM equations are developed from the original dissolution model using a volume averaging theory [46], taking into account the density variations with concentration. In Section 2.1, the original dissolution model is introduced. In Section 2.2, we present the upscaling method leading to the DIM equations.

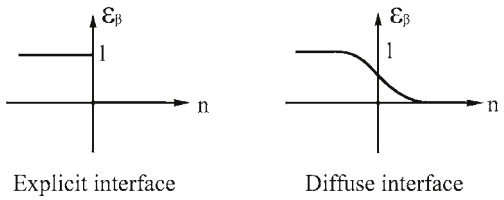

Fig. 2 Explicit and diffuse interfaces

2.1 Original multiphase model

Suppose the liquid phase β contains species A and B in a binary system and the solid phase σ contains only species A. We write the balance equations below.

The total mass balance equation for the β-phase is given by

$$\frac{\partial \rho_\beta}{\partial t} + \nabla \cdot \left(\rho_\beta \boldsymbol{v}_\beta\right) = 0 \tag{1}$$

The mass balance equations for species A and B in the β-phase are written as

$$\frac{\partial \left(\rho_\beta \omega_{A\beta}\right)}{\partial t} + \nabla \cdot \left(\rho_\beta \omega_{A\beta} \boldsymbol{v}_{A\beta}\right) = 0 \tag{2}$$

$$\frac{\partial \left(\rho_\beta \omega_{B\beta}\right)}{\partial t} + \nabla \cdot \left(\rho_\beta \omega_{B\beta} \boldsymbol{v}_{B\beta}\right) = 0 \tag{3}$$

where $\omega_{A\beta}$, $\omega_{B\beta}$ represent the mass fractions of species A and B, respectively.

The mass balance equation for the σ-phase is written as

$$\frac{\partial \rho_\sigma}{\partial t} + \nabla \cdot \left(\rho_\sigma \boldsymbol{v}_\sigma\right) = 0 \tag{4}$$

Generally, the solid phase is immobile; thus, $\boldsymbol{v}_\sigma = 0$. Here we keep $\boldsymbol{v}_\sigma$ during the development because this might be interesting for theoretical reasons, for instance to see the evolution of the dissolving surface in a frame moving with the average dissolution velocity such as in [44].

The Navier–Stokes equations for the β-phase are written as

$$\begin{aligned}&\frac{\partial \left(\rho_\beta \boldsymbol{v}_\beta\right)}{\partial t} + \nabla \cdot \left(\rho_\beta \boldsymbol{v}_\beta \boldsymbol{v}_\beta\right)\\ &\quad = -\left(\nabla p_\beta - \rho_\beta \boldsymbol{g}\right) + \mu_\beta \nabla^2 \boldsymbol{v}_\beta\end{aligned} \tag{5}$$

At the β–σ interface (denoted by $A_{\beta\sigma}$ in the following text), the chemical potentials for each species should be equal between the different phases. Therefore, for the special binary case under investigation, we have the following relations:

$$\tilde{\mu}_{A\beta}\left(\omega_{A\beta}, p, T\right) = \tilde{\mu}_{A\sigma}\left(\omega_{A\sigma}, p, T\right) \quad \text{at } A_{\beta\sigma} \tag{6}$$

where $\omega_{A\sigma}$ equals 1. It must be emphasized that in the complete binary case, i.e., when $\omega_{A\sigma} \neq 1$, there is also a relation similar to Eq. 6 for the other component.

This results in a classical equilibrium condition imposing an equilibrium concentration for species A, i.e.,

$$\omega_{A\beta} = \omega_{\text{eq}} \quad \text{at } A_{\beta\sigma} \tag{7}$$

The no-slip boundary condition at the β–σ interface gives:

$$\boldsymbol{v}_\beta - \boldsymbol{n}_{\beta\sigma}\boldsymbol{n}_{\beta\sigma} \cdot \boldsymbol{v}_\beta = 0 \quad \text{at } A_{\beta\sigma} \tag{8}$$

The mass balances for species A and B at the β–σ interface give:

$$\begin{aligned}&\rho_\beta \omega_{A\beta}\left(\boldsymbol{v}_{A\beta} - \boldsymbol{w}\right) \cdot \boldsymbol{n}_{\beta\sigma}\\ &\quad = \rho_\sigma \omega_{A\sigma}\left(\boldsymbol{v}_{A\sigma} - \boldsymbol{w}\right) \cdot \boldsymbol{n}_{\beta\sigma} \quad \text{at } A_{\beta\sigma}\end{aligned} \tag{9}$$

$$\begin{aligned}&\rho_\beta \omega_{B\beta}\left(\boldsymbol{v}_{B\beta} - \boldsymbol{w}\right) \cdot \boldsymbol{n}_{\beta\sigma}\\ &\quad = \rho_\sigma \omega_{B\sigma}\left(\boldsymbol{v}_{B\sigma} - \boldsymbol{w}\right) \cdot \boldsymbol{n}_{\beta\sigma} \quad \text{at } A_{\beta\sigma}\end{aligned} \tag{10}$$

and the total mass balance at the β–σ interface gives:

$$\rho_\beta\left(\boldsymbol{v}_\beta - \boldsymbol{w}\right) \cdot \boldsymbol{n}_{\beta\sigma} = \rho_\sigma\left(\boldsymbol{v}_\sigma - \boldsymbol{w}\right) \cdot \boldsymbol{n}_{\beta\sigma} \quad \text{at } A_{\beta\sigma} \tag{11}$$

where $\boldsymbol{w}$ represents the velocity of the interface and $\boldsymbol{v}_\sigma = \boldsymbol{v}_{A\sigma}$. As $\omega_{B\sigma} = 0$, the RHS term of Eq. 10 equals 0.

Equations 9 and 11 allow us to write the relation

$$\begin{aligned}&\rho_\beta \omega_{A\beta}\left(\boldsymbol{v}_{A\beta} - \boldsymbol{w}\right) \cdot \boldsymbol{n}_{\beta\sigma}\\ &\quad = \rho_\beta\left(\boldsymbol{v}_\beta - \boldsymbol{w}\right) \cdot \boldsymbol{n}_{\beta\sigma} \quad \text{at } A_{\beta\sigma}\end{aligned} \tag{12}$$

Using a theory of diffusion [36], we have

$$\rho_\beta \omega_{A\beta} \boldsymbol{v}_{A\beta} = \rho_\beta \omega_{A\beta} \boldsymbol{v}_\beta - \rho_\beta D_{A\beta} \nabla \omega_{A\beta} \tag{13}$$

and the left-hand side of Eq. 12 may be written as

$$\begin{aligned}&\boldsymbol{n}_{\beta\sigma} \cdot \rho_\beta \omega_{A\beta}\left(\boldsymbol{v}_{A\beta} - \boldsymbol{w}\right)\\ &\quad = \boldsymbol{n}_{\beta\sigma} \cdot \left(\rho_\beta \omega_{A\beta}\left(\boldsymbol{v}_\beta - \boldsymbol{w}\right) - \rho_\beta D_{A\beta} \nabla \omega_{A\beta}\right) \quad \text{at } A_{\beta\sigma}\end{aligned} \tag{14}$$

and Eq. 2 can also be transformed as

$$\frac{\partial \left(\rho_\beta \omega_{A\beta}\right)}{\partial t} + \nabla \cdot \left(\rho_\beta \omega_{A\beta} \boldsymbol{v}_\beta\right) = \nabla \cdot \left(\rho_\beta D_{A\beta} \nabla \omega_{A\beta}\right) \tag{15}$$

The whole balance equations presented above are sufficient to solve the physical problem, provided that the overall surrounding boundary conditions are also given. One substitutes Eq. 14 into Eq. 9 and with the help of Eq. 11, having

$$\boldsymbol{n}_{\beta\sigma} \cdot \boldsymbol{w} = \boldsymbol{n}_{\beta\sigma} \cdot \left(\boldsymbol{v}_\sigma + \frac{\rho_\beta}{\rho_\sigma\left(1 - \omega_{A\beta}\right)} D_{A\beta} \nabla \omega_{A\beta}\right) \quad \text{at } A_{\beta\sigma} \tag{16}$$

and

$$\boldsymbol{n}_{\beta\sigma} \cdot \boldsymbol{v}_\beta = \boldsymbol{n}_{\beta\sigma} \cdot \left(\boldsymbol{v}_\sigma + \frac{\rho_\beta - \rho_\sigma}{\rho_\sigma\left(1 - \omega_{A\beta}\right)} D_{A\beta} \nabla \omega_{A\beta}\right) \quad \text{at } A_{\beta\sigma} \tag{17}$$

It is emphasized here that for a tracer case ($\omega_{A\beta} \ll 1$), we recover the classical formation adopted by [15].

In summary, the above expressions give the recession velocity and the β-phase velocity at the interface, which are necessary to implement the direct explicit numerical methods, for instance, ALE.

2.2 Diffuse interface model based on a porous medium theory

Contrary to explicit methods who consider the interface as a discontinuous surface, a diffuse interface method regards the interface as a transition layer where the quantities vary rapidly but smoothly. The whole domain is considered to be a continuous medium without the direct distinction of solid or liquid, etc... Golfier et al. [15] studied one example of a local non-equilibrium dissolution model for porous media. It has the ability to be very close, with a proper choice of the exchange term (α) to the local equilibrium solution, which is equivalent to the original dissolution problems. Therefore, it is a good candidate for a diffuse interface model. We develop, in the section below, this model for dissolution including the effect of density variation. In our studied case, the σ-phase is immobile, i.e., $\boldsymbol{v}_\sigma = 0$ in the following analysis. The volume averaging theory [15, 27, 29, 46] will be used to upscale the balance equations.

According to the volume averaging theory, the averaged form of Eq. 2 can be expressed as

$$\frac{\partial \langle \rho_\beta \omega_{A\beta} \rangle}{\partial t} + \nabla \cdot \langle \rho_\beta \omega_{A\beta} \boldsymbol{v}_{A\beta} \rangle = -\frac{1}{V} \int_{A_{\beta\sigma}} \boldsymbol{n}_{\beta\sigma} \cdot \rho_\beta \omega_{A\beta} \left(\boldsymbol{v}_{A\beta} - \boldsymbol{w} \right) \mathrm{d}A \tag{18}$$

We define the average of the mass fraction as

$$\Omega_{A\beta} = \langle \omega_{A\beta} \rangle^\beta = \varepsilon_\beta^{-1} \langle \omega_{A\beta} \rangle = \frac{1}{V_\beta} \int_{V_\beta} \omega_{A\beta}(\boldsymbol{r}) \mathrm{d}V \tag{19}$$

and the average of the velocity as

$$\boldsymbol{V}_\beta = \langle \boldsymbol{v}_\beta \rangle = \varepsilon_\beta \langle \boldsymbol{v}_\beta \rangle^\beta = \frac{1}{V} \int_{V_\beta} \boldsymbol{v}_\beta(\boldsymbol{r}) \mathrm{d}V \tag{20}$$

where ε_β is the volume fraction of the β-phase, $\boldsymbol{V}_\beta$ is the filtration velocity and $\langle \boldsymbol{v}_\beta \rangle^\beta$ is the phase intrinsic average velocity.

The mathematical deduction of the DIM is presented in Appendix A. Finally, we have the form of the DIM including the mass balance equations for the β-phase, the σ-phase, and the species A in the β-phase, as presented below,

$$\frac{\partial \varepsilon_\beta \rho_\beta^*}{\partial t} + \nabla \cdot \left(\rho_\beta^* \boldsymbol{V}_\beta \right) = \rho_\beta^* \alpha (\omega_{\mathrm{eq}} - \Omega_{A\beta}) \tag{21}$$

$$-\rho_\sigma \frac{\partial \varepsilon_\sigma}{\partial t} = \rho_\sigma \frac{\partial \varepsilon_\beta}{\partial t} = \rho_\beta^* \alpha (\omega_{\mathrm{eq}} - \Omega_{A\beta}) \tag{22}$$

$$\varepsilon_\beta \rho_\beta^* \frac{\partial \Omega_{A\beta}}{\partial t} + \rho_\beta^* \boldsymbol{V}_\beta \cdot \nabla \Omega_{A\beta} = \nabla \cdot \left(\rho_\beta^* \boldsymbol{D}_{\boldsymbol{A\beta}}^* \cdot \nabla \Omega_{A\beta} \right) + \rho_\beta^* \alpha (1 - \Omega_{A\beta})(\omega_{\mathrm{eq}} - \Omega_{A\beta}) \tag{23}$$

where α refers to the exchange term between the β-phase and σ-phase, $\boldsymbol{D}_{\boldsymbol{A\beta}}^*$ represents the effective diffusion/dispersion coefficient, and the velocity, $\boldsymbol{V}_{\boldsymbol{\beta}}$, is calculated by the Darcy–Brinkman equation, as follows:

$$\frac{\mu_\beta^*}{\varepsilon_\beta} \Delta \boldsymbol{V}_\beta - \left(\nabla P_\beta - \rho_\beta^* \boldsymbol{g} \right) - \mu_\beta^* \boldsymbol{K}^{-1} \cdot \boldsymbol{V}_\beta = 0 \tag{24}$$

where the permeability, $\boldsymbol{K}$, is a function of the porosity ε_β. The Darcy–Brinkman equation will approach to Stokes equation when $\boldsymbol{K}$ is very large and will approach to Darcy's law when $\boldsymbol{K}$ is very small.

When α is infinite on the interface, the DIM equations should be able to recover the moving boundary velocity which is given by Eq. 16. To verify this point, a one-dimensional analytical solution is implemented in Appendix C to obtain the velocity of the moving boundary under the condition that α is infinite. The analytical solution reveals that the DIM agrees with the original model. In these equations, α is a crucial parameter since it will control the thickness of the diffuse interface. While such a model could have been guessed heuristically, there is some interest in using the proposed mathematical developments since they can be used as a guide to estimate the, somewhat "artificial," parameters in the equations. In Appendix B, we obtain the effective coefficients α and $\boldsymbol{D}_{\boldsymbol{A\beta}}^*$ by designing a unit cell as shown in Fig. 18 and by solving the closure problems with Eqs. 60–67. The solutions are given below. They are functions of ε_β.

$$\boldsymbol{D}_{A\beta}^* (\varepsilon_\beta) = \begin{bmatrix} \varepsilon_\beta D_{A\beta} & 0 \\ 0 & \varepsilon_\beta D_{A\beta} \left(1 + \frac{\mathrm{Pe}^2 \varepsilon_\beta^4}{1920 \eta^2} \right) \end{bmatrix} \tag{25}$$

$$\alpha\left(\varepsilon_\beta\right) = \frac{3}{l_c^2 \varepsilon_\beta} D_{A\beta} \tag{26}$$

$$\boldsymbol{K}\left(\varepsilon_\beta\right) = \frac{\varepsilon_\beta^2}{3 l_c^2} \boldsymbol{I} \tag{27}$$

$\boldsymbol{D}^*_{A\beta}$ represents the diffusion/dispersion tensor under the condition that the interface extends parallel to the y-axis. For a common case, we could follow the normal direction angle of the diffuse interface by looking at $\nabla\varepsilon_\beta/|\nabla\varepsilon_\beta|$. The corresponding diffusion tensor will be a "rotation" of the initial tensor that is represented by Eq. 71. Actually, the term which contains the Pe number is much smaller than 1 in most practical cases, provided that Pe is not too big. Here, the Péclet number is based on the unit cell characteristic length, which makes it close to a grid cell Péclet number. Keeping this number small enough is a good numerical practice, and we will assume that this condition is satisfied. In such cases, this term is negligible so that one does not need to do any rotation on this tensor.

α has a reciprocal relation with ε_β, as well as l_c^2. That is to say, the smaller the "porosity," the larger the mass exchange ability, or dissolution ability. When using this function, we have to modify its left value to avoid the value infinity. In addition, in Eq. 26, we have a constant coefficient that depends on l_c and $D_{A\beta}$. In the sequel of the paper, we simply introduce a constant and rewrite Eq. 26 as

$$\alpha\left(\varepsilon_\beta\right) = \alpha_0 \varepsilon_\beta^{-1} \tag{28}$$

The increasing of α_0 will sharpen the diffuse interface. The optimum choice of α_0 could be decided through simple numerical tests. Such tests will be done in the next section. Actually, as there is no real porous medium in the current problem, there may be various choices for α, e.g., polynomial, exponential functions of the porosity, etc., which could be designed freely, provided they maintain the properties of the diffuse interface (i.e., tendency to a finite, controlled thickness). In the tests presented in the next section, we will see that the choice of

$$\alpha\left(\varepsilon_\beta\right) = \alpha_0\left(1 - \varepsilon_\beta^\gamma\right) \tag{29}$$

is better than the original Eq. 28, where γ could probably range from 1 to 3, depending on the corresponding circumstances. The reason is that this kind of function has much less sharp variation near small ε_β, while keeping most of the features of Eq. 28. It is very helpful to the numerical stability of the simulations. More details will be presented in the next section.

3 Simulation examples

There are two purposes for the simulation tests presented in this section. First, we carry out a simple test to study the optimum choice of the exchange coefficient α for DIM. The reference field will be the results from ALE. The second objective of the tests is to validate the use of the DIM model for cases which are known to be difficult to solve, in particular cases with high Péclet and/or Rayleigh numbers. In such cases, the concentration gradients are very important near the dissolving interface where, because of the diffuse interface approach, the model departs from the true physical reality. It is important to verify that the DIM is able to reproduce the physics while maintaining its numerical advantages. Physical instabilities during the dissolution may be observed under certain conditions. In these tests, the software COMSOL™ will be used for both the DIM and ALE simulations. The major parameters used in the simulation examples are presented in Table 1,

3.1 Study of the influence of the exchange coefficient upon the interface displacement

In the last section, the effective coefficients, such as effective diffusion coefficient $D^*_{A\beta}$, exchange coefficient α, and effective permeability K, were obtained by using a volume averaging theory with an analysis of the closure problems upon a unit cell abstracted from a symmetrical plane-flow problem. Among the effective coefficients, the exchange coefficient is the most important parameter that influences the evolution of the interface displacement and thickness. It makes sense to implement the numerical tests with a plane-flow problem to study the influence of the exchange coefficient. Figure 3 presents the geometry of the simulation example, with length = 4 mm and width = 1 mm. The inlet velocity is set as 10^{-5} m/s, or Pe = 10.

3.1.1 Parameters that affects the interface thickness and displacement

The test adopts the effective coefficients given by Eqs. 83–85. An example of DIM results is shown in

Table 1 The parameters used for simulation examples

Parameter	Value	Unit
ρ_β	$1.0 \times 10^3(1 + 0.7385\omega_{A\beta})$	kg/m^3
ρ_σ	2.165×10^3	kg/m^3
μ_β	1.2×10^{-3}	kg/ms
D_{salt}	1.3×10^{-9}	m^2/s
ω_{eq}	0.27	–

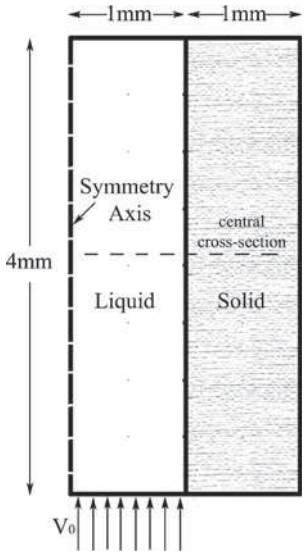

Fig. 3 The plane-flow geometry used for simulations

Fig. 4. The β-phase volume fraction, ε_β, is distributed continuously near the interface. We define the interface location at $\varepsilon_\beta = 0.5$ and the interface thickness as the distance between $\varepsilon_\beta = 0.2$ and $\varepsilon_\beta = 0.8$.

For comparison reasons, we also implemented an ALE simulation for this case. The ALE solution ($\omega_{A\beta}$ and boundary location) is plotted in Fig. 5. The solid–liquid boundary is represented explicitly, contrary to the diffuse interface under DIM. The computational domain expands to follow the moving of the interface. The ALE solution is used as a reference solution for DIM results. The detailed comparison of the interface locations between DIM and ALE will be presented in the section below. Before continuing the discussion, we must say a few words about the use of ALE simulation,

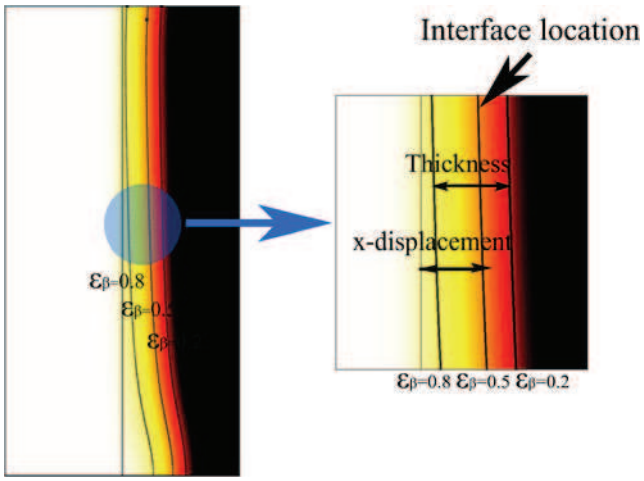

Fig. 4 ε_β distribution under a DIM simulation: the location and thickness of the diffuse interface

at least as it is implemented under COMSOL, i.e., without automatic remeshing. Surface imperfections are generated during the calculations due to severely deformed meshes. This may cause a non-convergence of the calculation. Therefore, one had to save data, remesh, and restart the computation after some small time. In short, the ALE simulation is very sensitive to the boundary geometry and the mesh shape. It works better for smooth interfaces and simple geometries, while the DIM is less sensitive to these aspects. The most important feature of DIM is the interface thickness, which mainly depends on the order of magnitude of the exchange coefficient. Figure 6 presents the interface thickness as a function of the non-dimensional exchange coefficient number, $\alpha_0 L^2/D_{\text{salt}}$ at a same time, measured at the central cross section. L represents the domain width. For very small α_0, the interface could not diffuse sufficiently as the solid–liquid mass exchange is very small. After a critical point, the increasing of α_0 sharpens the interface thickness, with a limit approaching to 0. In the limit α tends to infinity, when the solid phase is present, we obtain a so-called local equilibrium situation characterized by an infinitely thin interface and a concentration that reaches its equilibrium concentration at the interface, i.e., the mathematical solution of the original problems. Figure 7, which presents the evolution of the interface displacement at the central cross section as a function of α_0, shows that we need a limit value when increasing α_0, e.g., around $50 D_{\text{salt}}/L^2$ in this case. It is important to master these aspects when using DIM results to avoid unphysical solutions. For details, an approximative convergence for the interface displacement is observed after a critical value of α_0, where a plateau begins to rise with a very small slope. There seems to be a gap between the current DIM solution and the reference ALE result. While it is expected theoretically that the gap will decrease with very large α_0, it must be emphasized that, depending on the numerical algorithm, α_0 cannot be taken as large as wanted since numerical difficulties may occur. For instance, if using operator splitting, the ODE system for the calculation of ε_β and $\omega_{A\beta}$ becomes very stiff and may require very small time steps. In practice, the best choice would be to identify the plateau in Fig. 7 and takes a large enough α_0, but not too large. Further, an optimization for the function shape for α could be made to improve the convergence and accuracy of DIM. This point will be discussed later in the paper. The time evolution of the interface thickness is also very important. Figure 8 shows the interface evolution with time at the central cross section. We see that, after a short time evolution, the interface reaches a steady-state

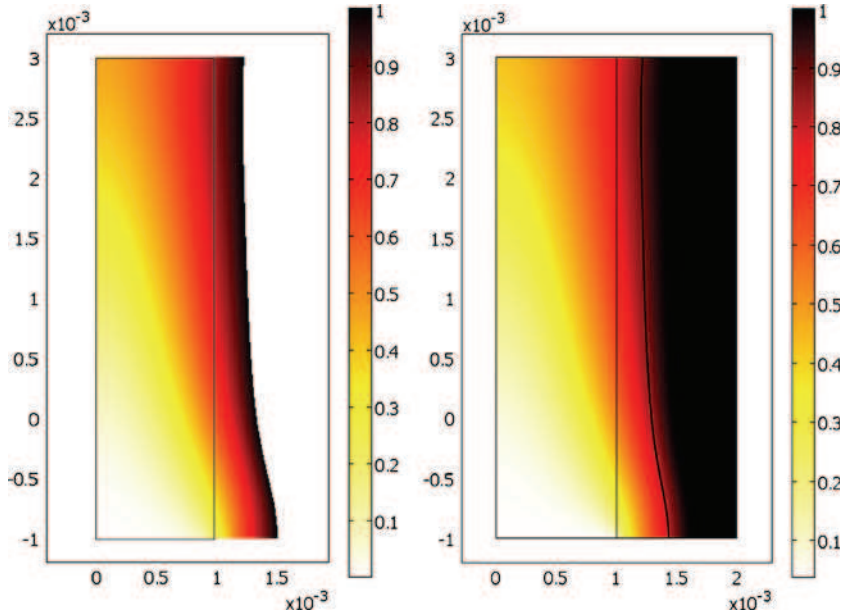

Fig. 5 $\omega_{A\beta}$ distribution and boundary location under the ALE (*left*) and DIM (*right*) simulations

value. This is an important feature of the DIM that the diffusion of the interface does not diverge. In practice, as shown in Fig. 6, the interface thickness depends on α_0. This is important also to quantify that since this will control mesh requirements (it is indeed necessary to have locally within the diffuse interface a small number of grid blocks, 3 seems to be an adequate minimum, numerically speaking). These simulations were carried out with a mesh size of 80×160. To study the mesh influence, Fig. 9 compares the interface displacement for two mesh sizes 80×160 and 160×320. The results show a very good grid convergence.

3.1.2 Interface displacement affected by various exchange coefficient functions

In the last section, the simulations were implemented using the exchange coefficient defined by Eq. 28. This expression is obtained from the closure problem with a unit cell abstracted from a plane flow. However, this curve is not practical for numerical simulations, as it approaches infinity near 0 and has very steep derivative when ε_β is small. Numerical divergence is easily aroused and a very small mesh size is required in such a case. Actually, since the choice for the effective

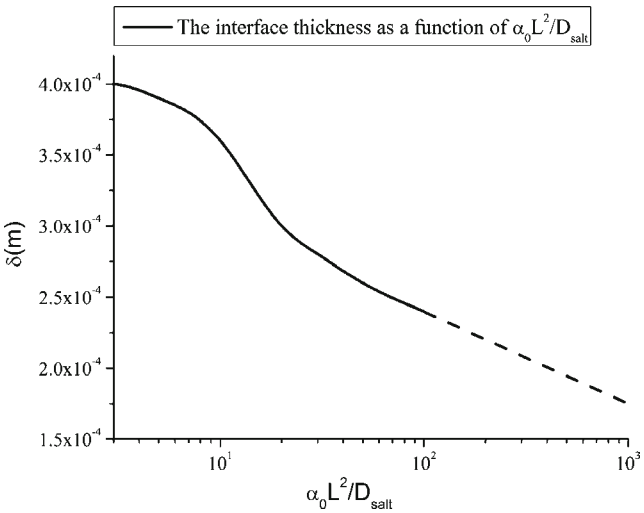

Fig. 6 The interface thickness as a function of α_0 at time $t =$ 1,000 s

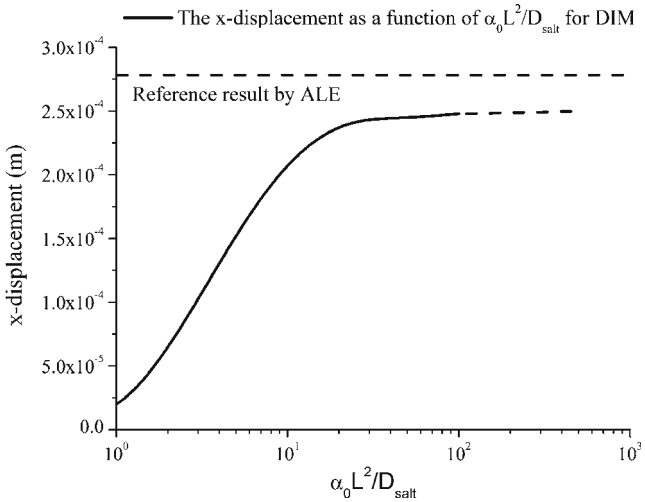

Fig. 7 The interface displacement as a function of α_0 at time $t =$ 1,000 s

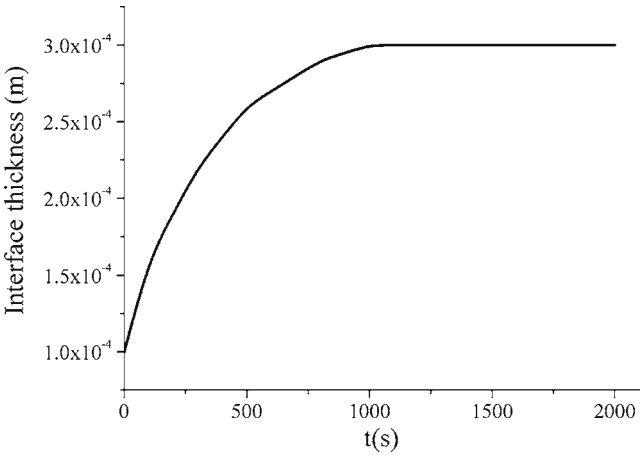

Fig. 8 The interface thickness as a function of time

coefficient is not highly constrained, without loss of significance, we tested new curves close to the reciprocal shape. Among them, four simple and representative curves will be used for comparison: (1) $\alpha = 4\alpha_0\varepsilon_\beta\left(1-\varepsilon_\beta\right)$, (2) $\alpha = \alpha_0\left(1-\varepsilon_\beta^2\right)$, (3) $\alpha = \alpha_0\left(1-\varepsilon_\beta\right)$, and (4) $\alpha = \alpha_0\left(1-\varepsilon_\beta\right)^2$. Simulations are carried out using these curves, respectively. For all these four cases above, we find that the critical values of α_0, which lead to an approximative convergence for the interface displacement, are on the order of $10D_{\text{salt}}/L^2$. To guarantee the accuracy of the results, we use $\alpha_0 = 10^2 D_{\text{salt}}/L^2$ for all these cases. The comparison among different solutions is presented in Fig. 10.

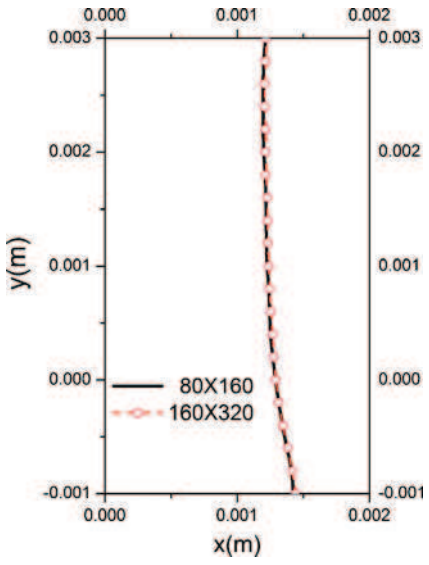

Fig. 9 Comparison of the interface location between the use of 80 × 160 and 160 × 320 mesh numbers

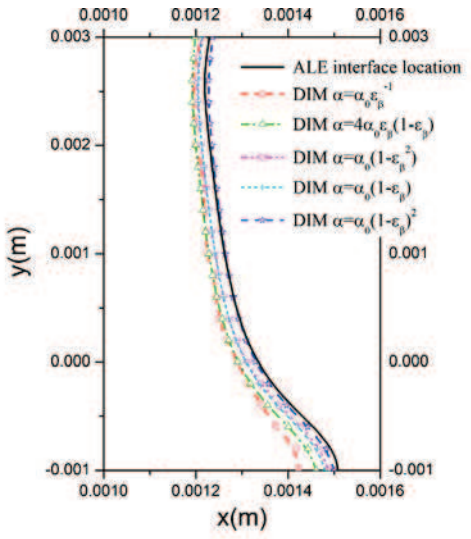

(a) Interface location at time t=1000s

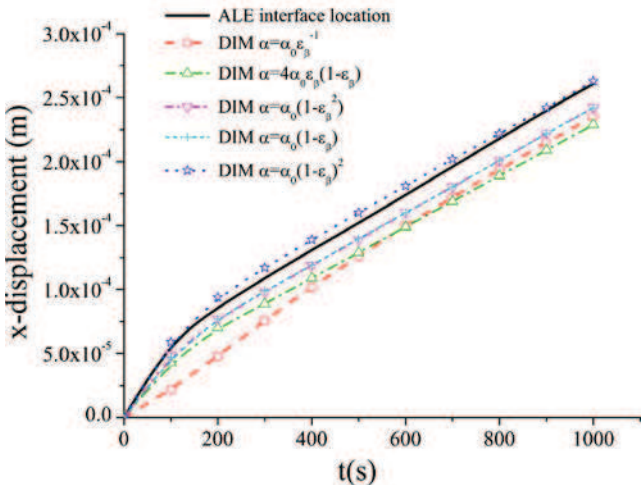

(b) Interface displacement as a function of time

Fig. 10 Comparison of the interface displacement among different exchange coefficients

The comparisons of the interface displacements show that the curve $\alpha = \alpha_0\left(1-\varepsilon_\beta\right)^2$ provides the best solution compared to the reference (ALE solution). In fact, this curve has well inherited the features of the reciprocal curve, for instance, with large values at small ε_β and small values at large ε_β, with positive second-order gradients in the whole domain. Therefore, it is not surprising to obtain a good approximation using this curve. The curve $\alpha = \alpha_0\varepsilon_\beta^{-1}$ obtained from the analytical approach gives an error up to about 20 %. The reason is that the mass exchange coefficients are too small in most regions. For the other curves, there are about 5–10 % errors compared to the reference solution. These errors are acceptable from a numerical point of view. Therefore, the curves such

as $\alpha = \alpha_0\left(1-\varepsilon_\beta^2\right)$ and $\alpha = \alpha_0\left(1-\varepsilon_\beta\right)$ are also good choices. We can also observe that the slope of the interface displacement with time in the reference solution is a little larger than that in the DIM simulations, with about 5 % difference between them. The reason is that in a practical DIM simulation, we could not use an infinite α_0 to approach the ultimate convergence. However, this error is tolerable with engineering requirement, while one can also benefit from a much smaller numerical requirement. It must be emphasized here that we discuss this comparison at the beginning of the dissolution process. At this very beginning, we have for DIM a double process: the recession of the interface and the thickening of the interface. Because of the transient behavior for the interface thickness, the relative error interface thickness/interface displacement is relatively large at the beginning. However, since the interface thickness reaches a constant value, this relative error decreases with time (after $t \geq 1{,}000$ s in the particular example).

In this paragraph, we discuss the definition of the interface location. The definition of the interface location as $\varepsilon_\beta = 0.5$ is somewhat instinctive. For a more strict identification, the interface location could be defined such that the integral of the solid volume fraction in the "liquid region" is equal to the integral of the liquid volume fraction in the "solid region", e.g.,

$$\int_{\Omega\in\Gamma_-} \varepsilon_\sigma \mathrm{d}V = \int_{\Omega\in\Gamma_+} \varepsilon_\beta \mathrm{d}V \tag{30}$$

where Γ represents the interface location, Γ_- refers to the so called "liquid region", and Γ_+ refers to the so-called solid region. We plot the distributions of ε_β and the mass exchange term $K_{\beta\sigma}$ for different exchange coefficients in Fig. 11.

For the case $\alpha = \alpha_0\varepsilon_\beta^{-1}$, the interface is much more diffusive than for all the other cases. The reason is that dissolution is very slow in the region where ε_β is large, resulting in a small amount of "solid mass fraction" lagging in the "liquid region." The interface location can be roughly defined at $\varepsilon_\beta = 0.5$. Concerning $K_{\beta\sigma}$, it is distributed irregularly, inclining toward the region where ε_β is small and mass exchange is more active. In such a case, good numerical convergence may not be easily obtained. For the case $\alpha = \alpha_0\left(1-\varepsilon_\beta\right)^2$, the interface is also diffusive compared with the other three cases, with a long tail in the "liquid region." The interface location defined by Eq. 30 is estimated to be at $\varepsilon_\beta = 0.6$. On the contrary, it is interesting to see that the maximum of $K_{\beta\sigma}$ is where ε_β is nearly 0.4. This kind of asymmetry is also due to the small α in the region where

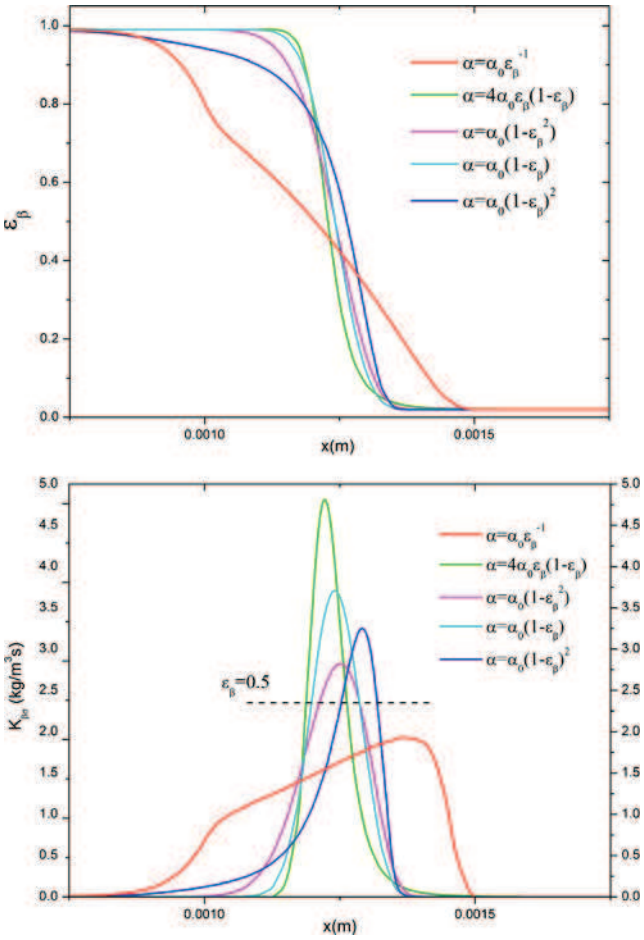

Fig. 11 Distributions of ε_β and $K_{\beta\sigma}$ under different exchange coefficients at the central cross section at time $t = 1{,}000$ s

ε_β is large. Therefore, the interface location for this case should be dragged leftward in Fig. 10. That is to say, the interface location is not so close to the reference solution as that defined at $\varepsilon_\beta = 0.5$. For the cases $\alpha = 4\alpha_0\varepsilon_\beta\left(1-\varepsilon_\beta\right)$, $\alpha = \alpha_0\left(1-\varepsilon_\beta^2\right)$, and $\alpha = \alpha_0\left(1-\varepsilon_\beta\right)$, it is found that the distributions of ε_β and $K_{\beta\sigma}$ are almost symmetric. Definitely, it is proper to define $\varepsilon_\beta = 0.5$ as the interface location in these cases. In such cases, the numerical convergence will also be good due to the smooth and symmetric evolution of those diffuse quantities. Furthermore, by reviewing the comparison in Fig. 10, we cannot distinguish a fundamental solution difference among these three cases. Anyhow, with the perspectives of inheriting the features from the function $\alpha = \alpha_0\varepsilon_\beta^{-1}$ obtained from the analytical approach, we recommend to adopt the function $\alpha = \alpha_0\left(1-\varepsilon_\beta^\gamma\right)$, where γ is greater than 1.

The above simulations are under the condition Pe = 10, which could be regarded as advection-controlled flow. We would also like to study the effects of these

different curves under diffusion-controlled situations. Figure 12 plots the interface displacement with time in a pure diffusive case. It is shown that the displacement with the curve $\alpha = \alpha_0 \left(1 - \varepsilon_\beta\right)^2$, $\alpha = \alpha_0 \left(1 - \varepsilon_\beta^2\right)$, and $\alpha = \alpha_0 \left(1 - \varepsilon_\beta\right)$ are all close to the ALE reference solution. One has to remember here that we look at the difference at the beginning of the dissolution process for which the interface thickening affects the interface location accuracy.

In summary, this section has intensively studied the influence of the exchange coefficients under several representative cases in both advection-controlled and diffusion-controlled situations. An optimum expression, $\alpha = \alpha_0 \left(1 - \varepsilon_\beta^\gamma\right)$, is proposed based on numerical tests, considering both the accuracy and stability reasons. We remind the reader that, by construction, the DIM does not require a particular value for the transport parameters. There is a lot of flexibility and the above indications are given to illustrate the possible choices.

3.2 Simulation with gravity effects

Whenever density variation is present in the fluid phases, buoyancy forces can play an important role, arousing physical instabilities. In this section, we test the ability of DIM to reproduce these physical phenomena. Figure 13 presents the geometry used for the simulations with gravity. The length and width of the domain are 15 and 6 mm, respectively. Pure water is injected with a constant velocity (U_0) into a channel whose walls are formed by two parallel salt blocks, resulting in the dissolution of the solid walls. Concerning the

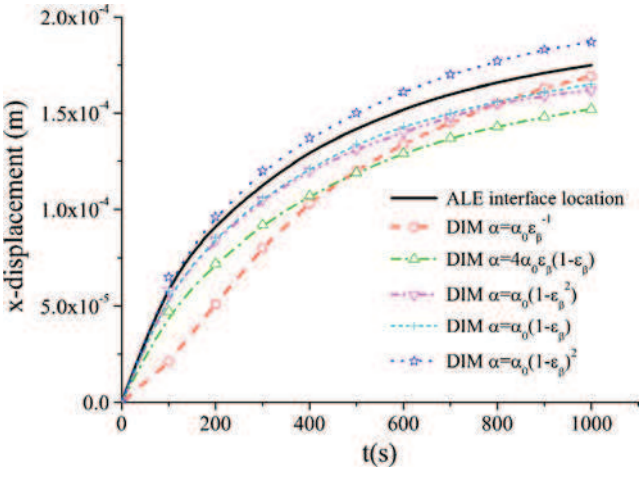

Fig. 12 Comparison of the interface displacement for different exchange coefficients in a pure diffusive case

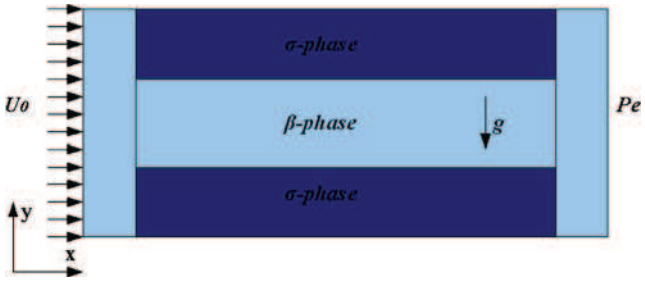

Fig. 13 The geometry used for the simulation with gravity effects

velocity, with $U_0 = 1.0 \times 10^{-6}$ m/s, the Péclet number calculated as $\mathrm{Pe} = U_0 L / D_{\mathrm{salt}}$ is close to unity, i.e., same importance of diffusion and advection mechanisms.

In this case, the dissolution of the salt walls results in higher concentrations around the interface than in other fluid regions. To characterize the gravity effects, we use the Rayleigh number, Ra, which is defined as the ratio of buoyancy forces to mass and momentum diffusivities

$$\mathrm{Ra} = \frac{\Delta\rho_{\beta\max} |\boldsymbol{g}| K_{\max} L}{\mu_\beta D_{A\beta}} \tag{31}$$

Here, $\Delta\rho_{\beta\max}$ represents the difference of the maximum and minimum fluid densities, $K_{\max}$ represents the maximum permeability, and L is the channel width.

Figure 14 plots the normalized mass fraction of species A, $\Omega_{A\beta}/\omega_{\mathrm{eq}}$. It shows that the symmetry of the flow and dissolution front is broken with important gravity effects. Gravity segregation appears at the cavity scale, and small-scale salt plumes are generated within the upper mass transport boundary layer through a natural convection mechanism. It is remarkable that these salt plumes affect the interface dissolution generating a rough interface. This kind of dissolution pattern was also observed experimentally [2, 10, 11].

Understanding the complex interaction of these roughnesses with the natural convection instabilities is beyond the scope of this paper, which is mainly on the model and its characteristics. In this section, we check that the convective structures do not suffer of numerical artifacts. In order to achieve this goal, we carried out several simulations with increasing α_0. The simulation results for $\Omega_{A\beta}/\omega_{\mathrm{eq}}$ are shown in Fig. 15. When α_0 is large enough, e.g., larger than $50 D_{\mathrm{salt}}/L^2$, the flow pattern does not change much with α_0, i.e., we have similar wavelet and salt finger distributions. The interface displacement is also not affected. With the decrease of α_0, e.g., when $\alpha_0 = 10 D_{\mathrm{salt}}/L^2$, the physical instabilities become smoothed, with fewer salt fingers and weaker tails. When α_0 is very small, no

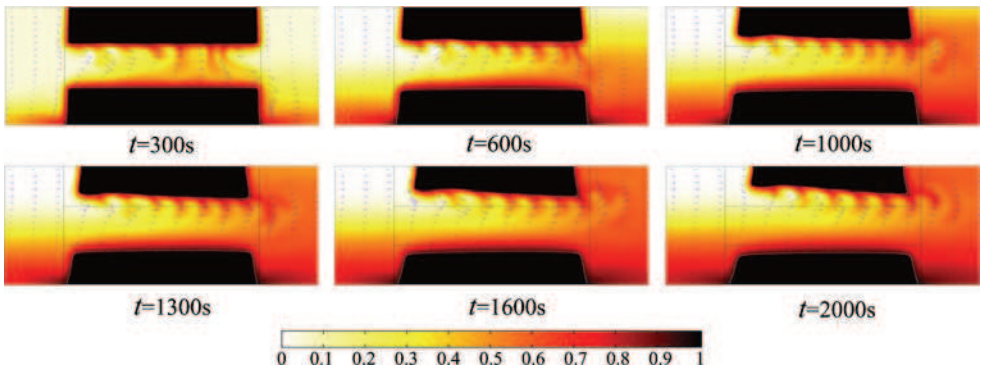

Fig. 14 Simulation results of $\Omega_{A\beta}/\omega_{\text{eq}}$ with time evolution under Pe = 10 and Ra = 100

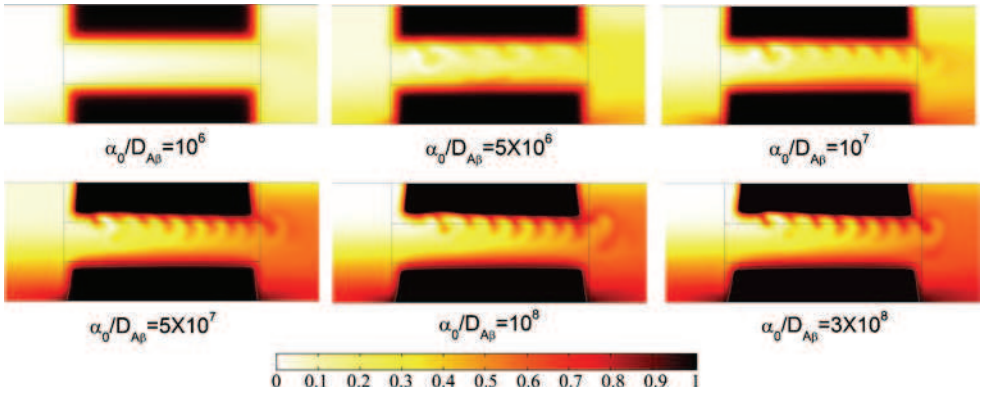

Fig. 15 Simulation results of $\Omega_{A\beta}/\omega_{\text{eq}}$ with different magnitudes of α_0 at time t = 1,000 s

instability could be observed. The averaged thickness of the diffuse interface as a function α_0 is plot in Fig. 16, showing that the averaged interface thickness is also reduced with the increase of α_0. This explains the smoothing of the instabilities when the interface thickness becomes larger: The local Rayleigh number within the boundary layer becomes smaller. Therefore, the physical instabilities observed in the simulations can be regarded as physically sounded without numerical flaws provided a correct value is taken for α_0.

It is also interesting to see the influences of gravity for different Ra numbers and Pe numbers. Figure 17 plots a diagram of simulation results for various Ra and Pe. Figure 17 briefly exhibits the trends corresponding to Ra and Pe variations. When Ra is zero or small, the fluid flow is almost symmetric and stable. With the increasing of Ra, natural convection is gradually strengthened and the physical instabilities become more and more strong and complex. In our examples, natural convection mostly happens around the upper interface rather than the bottom interface, as gravity and density gradients are in the same direction in the latter zone. Small-scale patterns, like wavelets around the interface, are observed. The number of wavelets increases when increasing the Ra number, greatly impacting the roughness of the interface during the dissolution. The role of the Péclet number is complex. On one hand, disturbances may be advected outside the domain of interest, which would result in an apparent increase in stability. On the other hand, a larger Péclet number means a thinner boundary layer, with larger density gradients in favor of a strong salt fingering mechanisms. While we clearly see that, for low Ra number, the

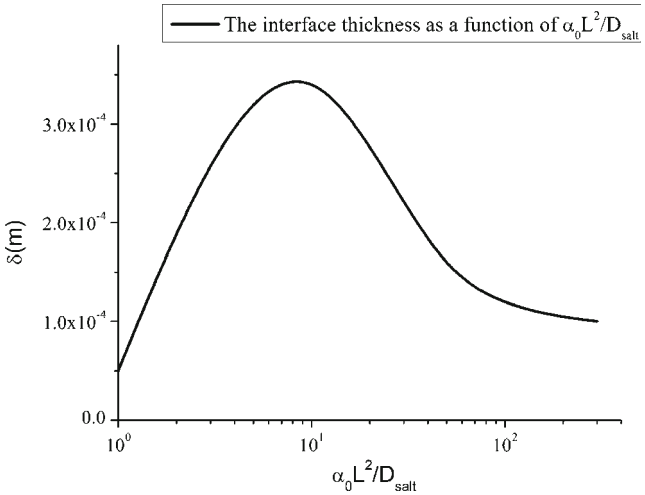

Fig. 16 Interface thickness with increasing α_0 at time t = 1,000 s

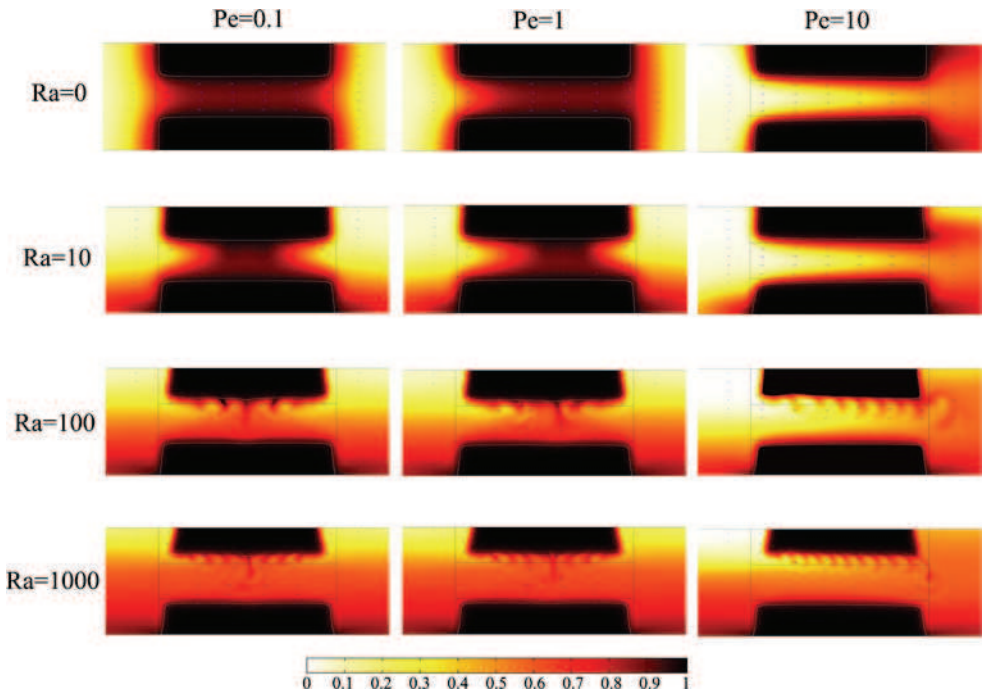

Fig. 17 Diagram for Pe–Ra

tube-scale convective pattern is "washed" out of the domain at large Péclet numbers, it does not mean that the occurrence of salt fingering is greatly affected at high Péclet numbers. Given the choice of a reference scale, i.e., the channel diameter, the geometry depends on a dimensionless ratio A. We did not explore different values of this ratio. Our particular choice $A = 5$ corresponds to a channel of relatively large extension, in order to be able to obtain several natural convection patterns at large Raleigh numbers. A thorough study of the impact of this parameter has to be undertaken but is beyond the scope of this paper. While the study of hydrodynamic instabilities has been very popular in many different domains, the coupling of natural convection and dissolution has received less attention and will remain our objective in future studies. We did not explore here very large Peclet numbers. In terms of the characteristics of the Pe–Ra diagram, we think that the various pattern limits have been explored. Higher Pe values would increase the "instability washing out" mechanism. However, very large Pe numbers will produce very thin boundary layers, and it will be necessary to verify that the interface thickness does not affect the accuracy of the dissolution modeling.

4 Conclusion

For simulations of the solid–liquid dissolution process, one can use either explicit treatment methods (represented by ALE in this paper) or diffuse interface methods (a local non-equilibrium DIM in this paper). ALE methods face difficulties when solving problems with complex interfaces, e.g., sharp angles, complex pore structures, as it relies strongly on the mesh shape. On the contrary, the DIM methods are easier to implement for simulating dissolution problems, as the whole domain is described through a phase field (volume fraction of liquid phase in this paper). In this paper, adopting the idea from [15], a local non-equilibrium diffuse interface model based on a porous medium theory is extended to study dissolution problems with density variations taken into account. A closure problem is solved with a unit cell abstracted from a plane flow to obtain the effective coefficients for the averaged equations, e.g., effective diffusion coefficient $D^*_{A\beta}$, exchange coefficient α. Several numerical tests with a plane-flow geometry were carried out to study the features of DIM simulations, for instance, the influence of the exchange coefficient magnitude and shape on the diffuse interface thickness and displacement. An "optimum" expression for the exchange coefficient was obtained by looking at the agreement between the DIM solutions and the reference ALE solutions.

Numerical tests showed the ability of DIM computations to reproduce conveniently flows with strong density variations, i.e., large Rayleigh numbers. Unstable flows producing salt fingers and interface wavelets were observed as a function of the Rayleigh number, Ra. Computations showed also the impact of the Péclet

number on the instabilities dynamic. A diagram illustrating the Ra–Pe interactions was proposed for flow in a tube-like domain.

It must be mentioned here that non-traditional terms in the macro-scale transport equations have been neglected in this study. Some non-linearities and dependences have also been discarded, like for instance dispersion mechanisms (Taylor dispersion for the plane unit cell). Would they improve the simulations, for instance by leading to a better convergence? We have not found evidence in preliminary tests. Of course, this is a different matter when the local non-equilibrium model is used for a true porous medium application, as illustrated in [14], for which the effective properties must be estimated accurately.

A further advantage of using a diffuse interface model is that it allows us to introduce easily automatic remeshing algorithms, such as adaptive mesh refinement (AMR) algorithms, which can greatly improve the calculation speed, since very fine meshes are required near the interface. The AMR algorithm for 2D and 3D simulations using the local non-equilibrium DIM will be presented in a subsequent paper.

Acknowledgment The authors would like to thank INERIS for the financial support.

Appendix A: Upscaling of the balance equations

Substituting Eqs. 13 and 14 into Eq. 18, we have

$$\underbrace{\frac{\partial \left\langle \rho_\beta \omega_{A\beta} \right\rangle}{\partial t}}_{[a]\ \text{accumulation}} + \underbrace{\nabla \cdot \left\langle \rho_\beta \omega_{A\beta} \boldsymbol{v}_\beta \right\rangle}_{[b]\ \text{advection}} = \underbrace{\nabla \cdot \left\langle \rho_\beta D_{A\beta} \nabla \omega_{A\beta} \right\rangle}_{[c]\ \text{diffusion}} \underbrace{- \frac{1}{V} \int_{A_{\beta\sigma}} \boldsymbol{n}_{\beta\sigma} \cdot \rho_\beta \left(\boldsymbol{v}_\beta - \boldsymbol{w} \right) \mathrm{d}A}_{[d]\ \text{phase exchange}} \tag{32}$$

We introduce the deviations of the mass fraction and velocity, respectively, by

$$\tilde{\omega}_{A\beta} = \omega_{A\beta} - \Omega_{A\beta} \tag{33}$$

$$\tilde{\boldsymbol{v}}_\beta = \boldsymbol{v}_\beta - \varepsilon_\beta^{-1} \boldsymbol{V}_\beta \tag{34}$$

Using a Taylor's series expansion, terms involving the density may be written

$$\begin{aligned} \left\langle \rho_\beta \omega_{A\beta} \right\rangle &= \left\langle \rho_\beta \left(\left\langle \omega_{A\beta} \right\rangle^\beta + \tilde{\omega}_{A\beta} \right) \omega_{A\beta} \right\rangle \\ &= \left\langle \left(\rho_\beta \left(\left\langle \omega_{A\beta} \right\rangle^\beta \right) + \frac{\partial \rho_\beta}{\partial \omega_{A\beta}} \tilde{\omega}_{A\beta} + \cdots \right) \omega_{A\beta} \right\rangle \end{aligned} \tag{35}$$

In Eq. 35, it can be demonstrated using the classical theory of dispersion that $\frac{\partial \rho_\beta}{\partial \omega_{A\beta}} \tilde{\omega}_{A\beta}$ has the order of $O\left(\frac{l}{L} \Omega_{A\beta}\right)$, so that when satisfying the constraint $O\left(\frac{l}{L} \Omega_{A\beta}\right) \ll \rho_\beta \left(\Omega_{A\beta}\right)$, Eq. 35 can be simplified to

$$\left\langle \left(\rho_\beta \left(\Omega_{A\beta} \right) + \frac{\partial \rho_\beta}{\partial \omega_{A\beta}} \tilde{\omega}_{A\beta} + \cdots \right) \omega_{A\beta} \right\rangle = \left\langle \rho_\beta \left(\Omega_{A\beta} \right) \omega_{A\beta} \right\rangle \tag{36}$$

Implementing a Taylor's expansion again for the spatial variations of the averaged quantities, we have

$$\begin{aligned} &\left\langle \rho_\beta \left(\Omega_{A\beta} \right) \omega_{A\beta} \right\rangle \\ &= \left\langle \rho_\beta \left(\Omega_{A\beta}|_{\boldsymbol{x}} + \boldsymbol{y} \cdot \nabla \Omega_{A\beta} + \frac{1}{2} \boldsymbol{y}\boldsymbol{y} : \nabla \nabla \Omega_{A\beta} + \cdots \right) \omega_{A\beta} \right\rangle \end{aligned} \tag{37}$$

Following the analysis of [28], Eq. 37 can be simplified to

$$\begin{aligned} &\left\langle \rho_\beta \left(\Omega_{A\beta}|_{\boldsymbol{x}} + \boldsymbol{y} \cdot \nabla \Omega_{A\beta} + \frac{1}{2} \boldsymbol{y}\boldsymbol{y} : \nabla \nabla \Omega_{A\beta} + \cdots \right) \omega_{A\beta} \right\rangle \\ &= \left\langle \rho_\beta \left(\Omega_{A\beta}|_{\boldsymbol{x}} \right) \omega_{A\beta} \right\rangle \\ &= \rho_\beta \left(\Omega_{A\beta} \right) \left\langle \omega_{A\beta} \right\rangle = \varepsilon_\beta \rho_\beta \left(\Omega_{A\beta} \right) \Omega_{A\beta} \end{aligned} \tag{38}$$

thus we can make the following simplification

$$\left\langle \rho_\beta \omega_{A\beta} \right\rangle = \varepsilon_\beta \rho_\beta^* \Omega_{A\beta} \tag{39}$$

where ρ_β^* represents $\rho_\beta \left(\Omega_{A\beta}\right)$.

Similarly, we can also obtain the simplifications:

$$\left\langle \rho_\beta \omega_{A\beta} \boldsymbol{v}_\beta \right\rangle = \rho_\beta^* \left\langle \omega_{A\beta} \boldsymbol{v}_\beta \right\rangle \tag{40}$$

$$\left\langle \rho_\beta D_{A\beta} \nabla \omega_{A\beta} \right\rangle = \rho_\beta^* \left\langle D_{A\beta} \nabla \omega_{A\beta} \right\rangle \tag{41}$$

This enables us to extend the term [a] in Eq. 32 as

$$[a] = \left(\varepsilon_\beta \rho_\beta^* \frac{\partial \Omega_{A\beta}}{\partial t} + \Omega_{A\beta} \frac{\partial \varepsilon_\beta \rho_\beta^*}{\partial t} \right) \tag{42}$$

Term [b] can be extended as

$$
\begin{aligned}
[b] &= \nabla \cdot \left\langle \rho_\beta \omega_{A\beta} \boldsymbol{v}_\beta \right\rangle \\
&= \nabla \cdot \left(\rho_\beta^* \left\langle \omega_{A\beta} \boldsymbol{v}_\beta \right\rangle \right) \\
&= \nabla \cdot \left(\rho_\beta^* \left(\Omega_{A\beta} \boldsymbol{V}_\beta + \left\langle \tilde{\omega}_{A\beta} \boldsymbol{v}_\beta \right\rangle \right) \right) \\
&= \Omega_{A\beta} \nabla \cdot \left(\rho_\beta^* \boldsymbol{V}_\beta \right) + \left(\rho_\beta^* \boldsymbol{V}_\beta \right) \cdot \nabla \Omega_{A\beta} \\
&\quad + \rho_\beta^* \nabla \cdot \left\langle \tilde{\omega}_{A\beta} \tilde{\boldsymbol{v}}_\beta \right\rangle + \left\langle \tilde{\omega}_{A\beta} \tilde{\boldsymbol{v}}_\beta \right\rangle \cdot \nabla \rho_\beta^*
\end{aligned} \tag{43}
$$

Term [c] can be extended as

$$
[c] = \nabla \cdot \left\langle \rho_\beta D_{A\beta} \nabla \omega_{A\beta} \right\rangle = \nabla \cdot \left(\rho_\beta^* \left\langle D_{A\beta} \nabla \omega_{A\beta} \right\rangle \right)
$$

$$
= \nabla \cdot \left[\rho_\beta^* D_{A\beta} \left(\nabla \left(\varepsilon_\beta \Omega_{A\beta} \right) + \frac{1}{V} \int\limits_{A_{\beta\sigma}} \boldsymbol{n}_{\beta\sigma} \omega_{A\beta} \mathrm{d}A \right) \right] \tag{44}
$$

$$
= \nabla \cdot \left[\rho_\beta^* D_{A\beta} \left(\varepsilon_\beta \nabla \Omega_{A\beta} + \frac{1}{V} \int\limits_{A_{\beta\sigma}} \boldsymbol{n}_{\beta\sigma} \tilde{\omega}_{A\beta} \mathrm{d}A \right) \right] \tag{45}
$$

According to Eqs. 16–17, term [d] can be extended as

$$
\begin{aligned}
[d] = K_{\beta\sigma} &= -\frac{1}{V} \int\limits_{A_{\beta\sigma}} \boldsymbol{n}_{\beta\sigma} \cdot \rho_\beta \left(\boldsymbol{v}_\beta - \boldsymbol{w} \right) \mathrm{d}A \\
&= \frac{1}{V} \int\limits_{A_{\beta\sigma}} \boldsymbol{n}_{\beta\sigma} \cdot \frac{\rho_\beta D_{A\beta}}{\left(1 - \omega_{A\beta} \right)} \nabla \omega_{A\beta} \mathrm{d}A
\end{aligned} \tag{46}
$$

where $K_{\beta\sigma}$ represents the exchange term between the σ-phase and the β-phase.

In a whole, Eq. 32 can be written as,

$$
\begin{aligned}
&\varepsilon_\beta \rho_\beta^* \frac{\partial \Omega_{A\beta}}{\partial t} + \Omega_{A\beta} \frac{\partial \varepsilon_\beta \rho_\beta^*}{\partial t} \\
&+ \Omega_{A\beta} \nabla \cdot \left(\rho_\beta^* \boldsymbol{V}_\beta \right) + \left(\rho_\beta^* \boldsymbol{V}_\beta \right) \cdot \nabla \Omega_{A\beta} \\
&+ \rho_\beta^* \nabla \cdot \left\langle \tilde{\omega}_{A\beta} \tilde{\boldsymbol{v}}_\beta \right\rangle + \left\langle \tilde{\omega}_{A\beta} \tilde{\boldsymbol{v}}_\beta \right\rangle \cdot \nabla \rho_\beta^* \\
&\quad = \nabla \cdot \rho_\beta^* D_{A\beta} \left(\varepsilon_\beta \nabla \Omega_{A\beta} + \frac{1}{V} \int\limits_{A_{\beta\sigma}} \boldsymbol{n}_{\beta\sigma} \tilde{\omega}_{A\beta} \mathrm{d}A \right) \\
&\qquad + K_{\beta\sigma}
\end{aligned} \tag{47}
$$

Similarly, we can also write the averaged form of the total mass continuity equation (Eq. 1) as,

$$
\frac{\partial \varepsilon_\beta \rho_\beta^*}{\partial t} + \nabla \cdot \left(\rho_\beta^* \boldsymbol{V}_\beta \right) = K_{\beta\sigma} \tag{48}
$$

Subtract $\Omega_{A\beta} \times$ Eq. 48 to Eq. 47, we obtain the averaged form of the balance equation as follows:

$$
\begin{aligned}
&\varepsilon_\beta \rho_\beta^* \frac{\partial \Omega_{A\beta}}{\partial t} + \left(\rho_\beta^* \boldsymbol{V}_\beta \right) \cdot \nabla \Omega_{A\beta} \rho_\beta^* \nabla \cdot \left\langle \tilde{\omega}_{A\beta} \tilde{\boldsymbol{v}}_\beta \right\rangle \\
&+ \left\langle \tilde{\omega}_{A\beta} \tilde{\boldsymbol{v}}_\beta \right\rangle \cdot \nabla \rho_\beta^* \\
&\quad = \nabla \cdot \left[\rho_\beta^* D_{A\beta} \left(\varepsilon_\beta \nabla \Omega_{A\beta} + \frac{1}{V} \int\limits_{A_{\beta\sigma}} \boldsymbol{n}_{\beta\sigma} \tilde{\omega}_{A\beta} \mathrm{d}A \right) \right] \\
&\qquad + \left(1 - \Omega_{A\beta} \right) K_{\beta\sigma}
\end{aligned} \tag{49}
$$

where

$$
\begin{aligned}
K_{\beta\sigma} = &\frac{1}{V} \int\limits_{A_{\beta\sigma}} \boldsymbol{n}_{\beta\sigma} \cdot \frac{\rho_\beta D_{A\beta}}{\left(1 - \omega_{A\beta} \right)} \nabla \Omega_{A\beta} \mathrm{d}A \\
&+ \frac{1}{V} \int\limits_{A_{\beta\sigma}} \boldsymbol{n}_{\beta\sigma} \cdot \frac{\rho_\beta D_{A\beta}}{\left(1 - \omega_{A\beta} \right)} \nabla \tilde{\omega}_{A\beta} \mathrm{d}A
\end{aligned} \tag{50}
$$

In order to develop an equation for the deviation of the mass fraction, we firstly subtract $\omega_{A\beta} \times$ Eq. 1 from Eq. 2 and obtain

$$
\frac{\partial \omega_{A\beta}}{\partial t} + \boldsymbol{v}_\beta \cdot \nabla \omega_{A\beta} = \nabla \cdot \left(\rho_\beta D_{A\beta} \nabla \omega_{A\beta} \right) \tag{51}
$$

Subtracting Eq. 49 $\times \left(\varepsilon_\beta \rho_\beta^* \right)^{-1}$ to Eq. 51, we have

$$
\begin{aligned}
&\frac{\partial \tilde{\omega}_{A\beta}}{\partial t} + \tilde{\boldsymbol{v}}_\beta \cdot \nabla \Omega_{A\beta} + \boldsymbol{v}_\beta \cdot \nabla \tilde{\omega}_{A\beta} \\
&= \varepsilon_\beta^{-1} \nabla \cdot \left\langle \tilde{\omega}_{A\beta} \tilde{\boldsymbol{v}}_\beta \right\rangle + \left(\varepsilon_\beta \rho_\beta^* \right)^{-1} \left\langle \tilde{\omega}_{A\beta} \tilde{\boldsymbol{v}}_\beta \right\rangle \cdot \nabla \rho_\beta^* \\
&\quad + \frac{1}{\rho_\beta^*} \nabla \cdot \left(\rho_\beta^* D_{A\beta} \nabla \tilde{\omega}_{A\beta} \right) \\
&\quad + \frac{1}{\rho_\beta^*} \nabla \cdot \left[\left(\rho_\beta^* - \rho_\beta \right) D_{A\beta} \nabla \omega_{A\beta} \right] \\
&\quad + \left(\varepsilon_\beta \rho_\beta^* \right)^{-1} \nabla \cdot \rho_\beta^* D_{A\beta} \left(\frac{1}{V} \int\limits_{A_{\beta\sigma}} \boldsymbol{n}_{\beta\sigma} \tilde{\omega}_{A\beta} \mathrm{d}A \right) \\
&\quad - \left(\varepsilon_\beta \rho_\beta^* \right)^{-1} \left(1 - \Omega_{A\beta} \right) K_{\beta\sigma}
\end{aligned} \tag{52}
$$

For $l \ll L$, it can be assumed that

$$\varepsilon_\beta^{-1}\nabla\cdot\left\langle\tilde{\omega}_{A\beta}\tilde{\boldsymbol{v}}_\beta\right\rangle \ll \boldsymbol{v}_\beta\cdot\nabla\tilde{\omega}_{A\beta} \tag{53}$$

$$\varepsilon_\beta^{-1}\nabla\cdot\left(\rho_\beta^* D_{A\beta}\frac{1}{V}\int\limits_{A_{\beta\sigma}}\boldsymbol{n}_{\beta\sigma}\tilde{\omega}_{A\beta}\mathrm{d}A\right) \ll \nabla\cdot\left(\rho_\beta^* D_{A\beta}\nabla\tilde{\omega}_{A\beta}\right) \tag{54}$$

It is also assumed that

$$\left(\varepsilon_\beta\rho_\beta^*\right)^{-1}\left\langle\tilde{\omega}_{A\beta}\tilde{\boldsymbol{v}}_\beta\right\rangle\cdot\nabla\rho_\beta^* \ll \varepsilon_\beta^{-1}\nabla\cdot\left\langle\tilde{\omega}_{A\beta}\tilde{\boldsymbol{v}}_\beta\right\rangle \tag{55}$$

$$\frac{1}{\rho_\beta^*}\nabla\cdot\left[\left(\rho_\beta^*-\rho_\beta\right)D_{A\beta}\nabla\omega_{A\beta}\right] \ll \frac{1}{\rho_\beta^*}\nabla\cdot\left(\rho_\beta^* D_{A\beta}\nabla\tilde{\omega}_{A\beta}\right) \tag{56}$$

Then we can simplify Eq. 52 to

$$\begin{aligned}\frac{\partial\tilde{\omega}_{A\beta}}{\partial t}+\tilde{\boldsymbol{v}}_\beta\cdot\nabla\Omega_{A\beta}+\boldsymbol{v}_\beta\cdot\nabla\tilde{\omega}_{A\beta}&=\frac{1}{\rho_\beta^*}\nabla\cdot\left(\rho_\beta^* D_{A\beta}\nabla\tilde{\omega}_{A\beta}\right)\\&\quad-\left(\varepsilon_\beta\rho_\beta^*\right)^{-1}\frac{1}{V}\int\limits_{A_{\beta\sigma}}\boldsymbol{n}_{\beta\sigma}\cdot\frac{\rho_\beta D_{A\beta}\nabla\tilde{\omega}_{A\beta}}{1-\omega_{\mathrm{eq}}}\mathrm{d}A\end{aligned} \tag{57}$$

We suppose that, in a unit cell, $\rho_\beta \simeq \rho_\beta^*$, so that the last term of the above equation can be replaced by

$$\begin{aligned}&\left(\varepsilon_\beta\rho_\beta^*\right)^{-1}\frac{1}{V}\int\limits_{A_{\beta\sigma}}\boldsymbol{n}_{\beta\sigma}\cdot\frac{\rho_\beta D_{A\beta}\nabla\tilde{\omega}_{A\beta}}{1-\omega_{\mathrm{eq}}}\mathrm{d}A\\&=\left(\varepsilon_\beta\right)^{-1}\frac{1}{V}\int\limits_{A_{\beta\sigma}}\boldsymbol{n}_{\beta\sigma}\cdot\frac{D_{A\beta}\nabla\tilde{\omega}_{A\beta}}{1-\omega_{\mathrm{eq}}}\mathrm{d}A\end{aligned} \tag{58}$$

In Eqs. 49 and 57, non-homogeneous terms can be viewed as source terms for $\tilde{\omega}_{A\beta}$, so that $\tilde{\omega}_{A\beta}$ can be represented by the following expression according to [27] analysis:

$$\tilde{\omega}_{A\beta} = \boldsymbol{b}_\beta\cdot\nabla\Omega_{A\beta}+s_\beta(\omega_{\mathrm{eq}}-\Omega_{A\beta}) \tag{59}$$

where $\boldsymbol{b}_\beta$ and s_β are the mapping variables of the closure problem of the mass fraction deviation. They obey two different closure problems (problem Ia and problem Ib) approximating Eq. 57 as presented below. In practice, starting with the work [15], we need to couple problems Ia and Ib, i.e., s_β appears in problem Ia.

Problem Ia

$$\begin{aligned}\tilde{\boldsymbol{v}}_\beta+\boldsymbol{v}_\beta\cdot\nabla\boldsymbol{b}_\beta&=\nabla\cdot\left(D_{A\beta}\nabla\boldsymbol{b}_\beta\right)\\&\quad-\varepsilon_\beta^{-1}\frac{1}{V}\int\limits_{A_{\beta\sigma}}\boldsymbol{n}_{\beta\sigma}\cdot D_{A\beta}\nabla\boldsymbol{b}_\beta\mathrm{d}A\end{aligned} \tag{60}$$

BC1

$$\boldsymbol{b}_\beta = 0 \text{ at } A_{\beta\sigma} \tag{61}$$

$$\boldsymbol{b}_\beta\left(\boldsymbol{r}+\boldsymbol{l}_i\right)=\boldsymbol{b}_\beta\left(\boldsymbol{r}\right),\ i=1,2,3 \tag{62}$$

$$\left\langle\boldsymbol{b}_\beta\right\rangle^\beta = 0 \tag{63}$$

Problem Ib

$$\begin{aligned}\boldsymbol{v}_\beta\cdot\nabla s_\beta&=\nabla\cdot\left(D_{A\beta}\nabla s_\beta\right)\\&\quad-\frac{1}{V}\int\limits_{A_{\beta\sigma}}\boldsymbol{n}_{\beta\sigma}\cdot D_{A\beta}\nabla s_\beta\mathrm{d}A\end{aligned} \tag{64}$$

BC2

$$s_\beta = 1 \text{ at } A_{\beta\sigma} \tag{65}$$

$$s_\beta\left(\boldsymbol{r}+\boldsymbol{l}_i\right)=s_\beta\left(\boldsymbol{r}\right),\ i=1,2,3 \tag{66}$$

$$\left\langle s_\beta\right\rangle^\beta = 0 \tag{67}$$

Using these above forms in Eq. 49 leads to the following averaged equation form for the dissolution problem:

$$\begin{aligned}&\varepsilon_\beta\rho_\beta^*\frac{\partial\Omega_{A\beta}}{\partial t}+\rho_\beta^*(\boldsymbol{V}_\beta-(1-\Omega_{A\beta})\boldsymbol{u_{1\beta}}+D_{A\beta}\nabla\varepsilon_\beta)\\&\cdot\nabla\Omega_{A\beta}-\rho_\beta^*\nabla\cdot\left(\boldsymbol{d}_\beta\Omega_{A\beta}\right)\\&=\nabla\cdot\left(\varepsilon_\beta\rho_\beta^*\boldsymbol{D^*_{A\beta}}\cdot\nabla\Omega_{A\beta}\right)+(1-\Omega_{A\beta})K_{\beta\sigma}\end{aligned} \tag{68}$$

with

$$\begin{aligned}\boldsymbol{u_{1\beta}}&=\frac{1}{\rho_\beta^*}\frac{1}{V}\int\limits_{A_{\beta\sigma}}\frac{\rho_\beta}{\left(1-\omega_{\mathrm{eq}}\right)}D_{A\beta}\boldsymbol{n}_{\beta\sigma}\\&\quad\cdot\left[\nabla\boldsymbol{b}_\beta+\left(1-s_\beta\right)\boldsymbol{I}\right]\mathrm{d}A\end{aligned} \tag{69}$$

$$\boldsymbol{d}_\beta = -\frac{1}{V}\int\limits_{A_{\beta\sigma}}D_{A\beta}\left(\boldsymbol{n}_{\beta\sigma}s_\beta\right)\mathrm{d}A+\left\langle s_\beta\tilde{\boldsymbol{v}}_\beta\right\rangle \tag{70}$$

$$\boldsymbol{D}^{*}_{A\beta} = \varepsilon_\beta D_{A\beta}\left(\boldsymbol{I} + \varepsilon_\beta^{-1}\frac{1}{V}\int\limits_{A_{\beta\sigma}}\left(\boldsymbol{n}_{\beta\sigma}\boldsymbol{b}_\beta\right)\mathrm{d}A\right) - \varepsilon_\beta^{-1}\left\langle \boldsymbol{b}_\beta\tilde{\boldsymbol{v}}_\beta\right\rangle \tag{71}$$

$$K_{\beta\sigma} = \left[\alpha_1 + (1-\Omega_{A\beta})^{-1}\alpha_2\right](\omega_{\mathrm{eq}} - \Omega_{A\beta}) \tag{72}$$

$$\alpha_1 = \frac{1}{V}\int\limits_{A_{\beta\sigma}}\frac{\rho_\beta}{(1-\omega_{\mathrm{eq}})}D_{A\beta}\left(\boldsymbol{n}_{\beta\sigma}\cdot\nabla s_\beta\right)\mathrm{d}A \tag{73}$$

$$\alpha_2 = \nabla\rho^{*}_\beta\cdot\left\langle s_\beta\tilde{\boldsymbol{v}}_\beta\right\rangle \tag{74}$$

Since our only goal is to obtain a diffuse interface model, it is not necessary to keep all the features of the Darcy-scale non-equilibrium model. Therefore, in order to simplify the diffuse interface model, we neglect the terms $\boldsymbol{u_{1\beta}}$, $\boldsymbol{d}_\beta$, α_2 and $D_{A\beta}\nabla\varepsilon_\beta$. Consequently, Eq. 75 can be simplified as

$$\varepsilon_\beta\rho^{*}_\beta\frac{\partial\Omega_{A\beta}}{\partial t} + \rho^{*}_\beta\boldsymbol{V}_\beta\cdot\nabla\Omega_{A\beta} = \nabla\cdot\left(\rho^{*}_\beta\boldsymbol{D}^{*}_{A\beta}\cdot\nabla\Omega_{A\beta}\right) + (1-\Omega_{A\beta})K_{\beta\sigma} \tag{75}$$

where

$$K_{\beta\sigma} = \left[\frac{1}{V}\int\limits_{A_{\beta\sigma}}\frac{\rho_\beta}{(1-\omega_{\mathrm{eq}})}D_{A\beta}\left(\boldsymbol{n}_{\beta\sigma}\cdot\nabla s_\beta\right)\mathrm{d}A\right]\times\left(\omega_{\mathrm{eq}} - \Omega_{A\beta}\right) = \alpha(\omega_{\mathrm{eq}} - \Omega_{A\beta}) \tag{76}$$

Concerning the σ-phase, the upscaling method applied to Eq. 4 leads to

$$\frac{\partial\varepsilon_\sigma\langle\rho_\sigma\rangle^{\sigma}}{\partial t} = \frac{1}{V}\int\limits_{A_{\beta\sigma}}\rho_\sigma\boldsymbol{n}_{\sigma\beta}\cdot\boldsymbol{w}\mathrm{d}A \tag{77}$$

Since ρ_σ is a constant and $\varepsilon_\beta + \varepsilon_\sigma = 1$, according to Eq. 9, we rewrite the last equation as

$$\rho_\sigma\frac{\partial\varepsilon_\beta}{\partial t} = \frac{1}{V}\int\limits_{A_{\beta\sigma}}\boldsymbol{n}_{\beta\sigma}\cdot\boldsymbol{w}\mathrm{d}A = K_{\beta\sigma}. \tag{78}$$

Appendix B: Analysis for the effective coefficients

To obtain the estimates of the effective coefficients for solid–liquid dissolution problems, we consider a simple unit cell as represented in Fig 18. ε_β could be computed as l_β/l_{c}, where l_{c} is regarded as the characteristic length of the unit cell.

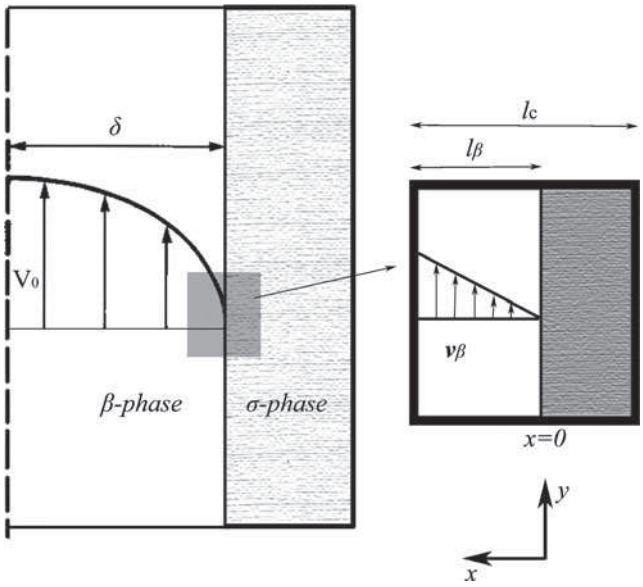

Fig. 18 A unit cell used for solid–liquid interface dissolution

In a domain including the interface, we have mass and momentum boundary layers that develop (Fig. 18), and we will make the simplification in the unit cell that the velocity v_β has a linear distribution against x in the unit cell. Therefore, we have the following expressions for v_β:

$$v_\beta = V_0 x/\delta = \mathrm{Pe}D_{A\beta}x/\delta^2 \tag{79}$$

Replacing this equation into the closure problems Eqs. 60–67, we are able to obtain the solutions for the closure variables, $\boldsymbol{b}_\beta$ and s_β, expressed as,

$$b_{\beta x} = 0 \tag{80}$$

$$b_{\beta y} = \frac{\mathrm{Pe}\left(16X^3 - 21\varepsilon_\beta X^2 + 6\varepsilon_\beta^2 X\right)}{96\eta} \tag{81}$$

$$s_\beta = \frac{\left(3X^2 - 6\varepsilon_\beta X + 2\varepsilon_\beta^2\right)}{2\varepsilon_\beta^2} \tag{82}$$

where $X = x/l_{\mathrm{c}}$ and $\eta = \delta/l_{\mathrm{c}}$.

Substituting the last three equations into Eq. 71 and Eq. 73, we have the following expressions for the effective diffusion coefficient and the exchange term,

$$\boldsymbol{D}^{*}_{A\beta} = \begin{bmatrix}\varepsilon_\beta D_{A\beta} & 0\\ 0 & \varepsilon_\beta D_{A\beta}\left(1 + \frac{\mathrm{Pe}^2\varepsilon_\beta^4}{1920\eta^2}\right)\end{bmatrix} \tag{83}$$

$$\alpha = \frac{3}{l_{\mathrm{c}}^2\varepsilon_\beta}D_{A\beta} \tag{84}$$

The effective permeability can also be obtained by the traditional upscaling,

$$\boldsymbol{K} = \frac{\varepsilon_\beta^2}{3l_c^2}\boldsymbol{I}. \tag{85}$$

Appendix C: 1D analytical solution of DIM equations

We define a diffuse interface zone Z_{DI} with thickness δ, where the left boundary approximates $\varepsilon_\beta = 0$ and the right boundary approximates $\varepsilon_\beta = 1$. When the mass exchange coefficient α is infinite, δ approaches to 0 and $\Omega_{A\beta}$ approaches to ω_{eq} in Z_{DI}. Consequently, an integration of Eq. 22 over Z_{DI} leads to,

$$\rho_\sigma \delta \frac{\mathrm{d}\varepsilon_\beta}{\mathrm{d}t} = K_{\beta\sigma} \tag{86}$$

where $K_{\beta\sigma} = \int_{Z_{\text{DI}}} \rho_\beta \alpha \left(\omega_{\text{eq}} - \Omega_{A\beta}\right) \mathrm{d}Z$ is the integration of the mass exchange in Z_{DI}. According to the mass balance, the speed of moving boundary $\boldsymbol{w}$ can be expressed as,

$$\boldsymbol{w} = -\delta \frac{\mathrm{d}\varepsilon_\beta}{\mathrm{d}t} \tag{87}$$

Equations 86 and 87 lead to the following relation,

$$\boldsymbol{w} = -\frac{1}{\rho_\sigma} K_{\beta\sigma} \tag{88}$$

Integrating of Eq. 21 over Z_{DI}, we have

$$\begin{aligned} &-\rho_\beta \boldsymbol{w} + \left(\rho_\beta \boldsymbol{V}_\beta\right)|_{Z_-}^{Z_+} \\ &\quad = -\rho_\beta \boldsymbol{w} + \left(\rho_\beta \boldsymbol{V}_\beta\right)_{Z_+} - \left(\rho_\beta \boldsymbol{V}_\beta\right)_{Z_-} = K_{\beta\sigma} \end{aligned} \tag{89}$$

Since $\boldsymbol{V}_\beta$ equals zero in the solid domain and equals $\boldsymbol{V}$ (velocity going out of the interface) in the liquid domain, Eq. 89 can be rewritten as,

$$-\rho_\beta \boldsymbol{w} + \rho_\beta \boldsymbol{V} = K_{\beta\sigma} \tag{90}$$

Multiply Eq. 21 with $\Omega_{A\beta}$ and add to Eq. 23, then integrating over Z_{DI}, we have

$$\begin{aligned} &\frac{\partial \varepsilon_\beta \rho_\beta \Omega_{A\beta}}{\partial t}\delta + \left(\rho_\beta \boldsymbol{V}_\beta \Omega_{A\beta}\right)|_{Z_-}^{Z_+} \\ &\quad = \left(\varepsilon_\beta \rho_\beta D_{A\beta} \nabla \Omega_{A\beta}\right)|_{Z_-}^{Z_+} + K_{\beta\sigma} \end{aligned} \tag{91}$$

or

$$-\Omega_{A\beta}\rho_\beta \boldsymbol{w} + \Omega_{A\beta}\rho_\beta \boldsymbol{V} = \rho_\beta D_{A\beta} \nabla \Omega_{A\beta} + K_{\beta\sigma} \tag{92}$$

Arranging Eqs. 88, 90, and 92, we have

$$\boldsymbol{w} = \frac{\rho_\beta}{\rho_\sigma (1 - \omega_{\text{eq}})} D_{A\beta} \nabla \Omega_{A\beta} \tag{93}$$

which has the same form as Eq. 16.

References

1. Anderson, D.M., McFadden, G.B.: Diffuse-interface methods in fluid mechanics. Annu. Rev. Fluid Mech. **30**, 139–165 (1998)
2. Anderson, R.Y., Kirkland, D.W.: Dissolution of salt deposits by brine density flow. Geology **8**, 66–69 (1980)
3. Beckermann, C., Diepers, H.-J., Steinbach, I., Karma, A., Tong, X.: Modeling melt convection in phase-field simulations of solidification. J. Comput. Phys. **154**, 468–496 (1999)
4. Bekri, S., Thovert, J.F., Adler, P.M.: Dissolution of porous media. Chem. Eng. Sci. **50**, 2765–2791 (1995)
5. Boettinger, W.J., Warren, J.A., Beckermann, C., Karma, A.: Phase-field simulation of solidification. Annu. Rev. Mater. Res. **32**, 163–194 (2002)
6. Bousquet-Melou, P., Neculae, N., Goyeau, B., Quintard, M.: Averaged solute transport during solidification of a binary mixture: active dispersion in dendritic structures. Metall. Mater. Trans. B **33**, 365–376 (2002)
7. Cahn, J.W., Hilliard, J.: Free energy of a nonuniform system. I. Interfacial free energy. J. Chem. Phys. **28**, 258–267 (1958)
8. Collins, J.B., Levine, H.: Diffuse interface model of diffusion-limited crystal growth. Phys. Rev. B **31**, 6119–6122 (1985)
9. Dell'Isola, F., Gouin, H., Rotoli, G.: Nucleation of spherical shell-like interfaces by second gradient theory: numerical simulations. Eur. J. Mech. B Fluid **15**, 545–568 (1996)
10. Dijk, P.E., Berkowitz, B.: Buoyancy-driven dissolution enhancement in rock fractures. Geology **28**, 1051–1054 (2000)
11. Dijk, P.E., Berkowitz, B., Yechieli, Y.: Measurement and analysis of dissolution patterns in rock fractures. Water Resour. Res. **38** (2002). doi:10.1029/2001WR000246
12. Donea, J., Giuliani, S., Halleux J.P.: An arbitrary Lagrangian–Eulerian finite element method for transient dynamic fluid–structure interactions. Comput. Methods Appl. Mech. Eng. **33**, 689–723 (1982)
13. Glimm, J., Grove, J.W., Li, X.L., Shyue, K.M., Zeng, Y., Zhang, Q.: Three-dimensional front tracking. SIAM J. Sci. Comput. **3**, 703–727 (1998)
14. Golfier, F., Quintard, M., Whitaker, S.: Heat and mass transfer in tubes: an analysis using the method of volume averaging. J. Porous Media **5**(3), 169–185 (2002)
15. Golfier, F., Zarcone, C., Bazin, B., Lenormand, R., Lasseux, D., Quintard, M.: On the ability of a Darcy-scale model to capture wormhole formation during the dissolution of a porous medium. J. Fluid Mech. **457**, 213–254 (2002)
16. Hirt, C.W., Nicolas, B.D.: Volume of fluid (VOF) method for the dynamics of free boundaries. J. Comput. Phys. **39**, 201–225 (1981)
17. Kang, Q., Zhang, D., Chen, S.: Simulation of dissolution and precipitation in porous media. J. Geophys. Res. **108**, 2505 (2003). doi:10.1029/2003JB002504
18. Kovacevic, I., Sarlera, B.: Solution of a phase-field model for dissolution of primary particles in binary aluminum alloys by an r-adaptive mesh-free method. Mater. Sci. Eng. A **413**, 423–428 (2005)
19. Leo, P.H., Lowengrub, J.S., Jou, H.J.: A diffuse interface model for microstructural evolution in elastically stressed solids. Acta Mater. **46**, 2113–2130 (1998)
20. Lopez, J., Hernandez, J., Gomez, P., Faura, F.: An improved PLIC-VOF method for tracking thin fluid structures in incompressible two-phase flows. J. Comput. Phys. **208**(1), 51–74 (2005)

21. Mao, X., Prommer, H., Barry, D.A., Langevin, C.D., Panteleit, B., Li, L.: Three-dimensional model for multi-component reactive transport with variable density groundwater flow. Environ. Modell. Softw. **21**, 615–628 (2006)
22. Maury, B.: Characteristics ale method for the unsteady 3d Navier–Stokes equations with a free surface. Int. J. Comput. Fluid Dyn. **6**, 175–188 (1996)
23. Mittal, R., Iaccarino, G.: Immersed boundary methods. Annu. Rev. Fluid Mech. **37**, 239–261 (2005)
24. Olsson, E., Kreiss, G.: A conservative level set method for two phase flow. J. Comput. Phys. **210**, 225–246 (2005)
25. Onuki, A., Kawasaki, K.: Nonequilibrium steady state of critical fluids under shear flow: a renormalization group approach. Ann. Phys. **121**, 456–528 (1979)
26. Osher, S., Fedkiw, R.: Level set methods: an overview and some recent results. J. Comput. Phys. **169**, 463–502 (2001)
27. Quintard, M., Whitaker, S.: Convection, dispersion, and interfacial transport of contaminant: homogeneous porous media. Adv. Water Resour. **17**, 221–239 (1994)
28. Quintard, M., Whitaker, S.: Transport in ordered and disordered porous media 1: the cellular average and the use of weighting functions. Transp. Porous Media **14**, 163–177 (1994)
29. Quintard, M., Whitaker, S.: Dissolution of an immobile phase during flow in porous media. Ind. Eng. Chem. Res. **38**, 833–844 (1999)
30. Rider, W.J., Kothe, D.B.: Reconstructing volume tracking. J. Comput. Phys. **141**(2), 112–152 (1998)
31. Roux, P., Goyeau, B., Gobin, D., Fichot, F., Quintard, M.: Chemical non-equilibrium modelling of columnar solidification. Int. J. Heat Mass Transfer **49**(23–24), 4496–4510 (2006)
32. Sekerka, R.F.: Morphology: from sharp interface to phase field models. J. Cryst. Growth **264**, 530–540 (2004)
33. Seppecher, P.: Moving contact lines in the Cahn–Hilliard theory. Int. J. Eng. Sci. **34**, 977–992 (1996)
34. Sethian, J.A., Smereka, P.: Level set methods for fluid interfaces. Annu. Rev. Fluid Mech. **35**, 341–372 (2003)
35. Stone, H.A., Leal, L.G.: The effects of surfactants on drop deformation and breakup. J. Fluid Mech. **220**, 161–186 (1990)
36. Taylor, R., Krishna, R.: Multicomponent Mass Transfer. Wiley-Interscience, New York (1993)
37. Teigen, K.E., Li, X., Lowengrub, J., Wang, F., Voigt, A.: A diffuse-interface approach for modelling transport, diffusion and adsorption/desorption of material quantities on a deformable interface. Commun. Math. Sci. **7**, 1009–1037 (2009)
38. Tiadena, J., Nestlerb, B., Diepersa, H.J., Steinbacha, I.: The multiphase-field model with an integrated concept for modelling solute diffusion. Physica D Nonlinear Phenom. **115**, 73–86 (1998)
39. Tryggvason, G., Bunner, B., Esmaeeli, A., Juric, D., Al-Rawahi, N., Tauber, W., Han, J., Nas, S., Jan, Y.-J.: A front-tracking method for the computations of multiphase flow. J. Comput. Phys. **169**, 708–759 (2001)
40. Turski, L.A., Langer, J.S.: Dynamics of a diffuse liquid–vapor interface. Phys. Rev. A **22**, 2189–2195 (1980)
41. van Noorden, T.L.: Crystal precipitation and dissolution in a porous medium: effective equations and numerical experiments. Multiscale Model. Simul. **7**, 1220–1236 (2009)
42. van Noorden, T.L., Eck, C.: Phase field approximation of a kinetic moving-boundary problem modelling dissolution and precipitation. Interfaces Free Bound. **13**, 29–55 (2011)
43. vanderWaals, J.D.: The thermodynamic theory of capillarity under the hypothesis of a continuous variation of density (translated by J.S. Rowlinson, 1893). J. Stat. Phys. **20**, 197–244 (1979)
44. Vignoles, G.L., Aspa, Y., Quintard, M.: Modelling of carbon–carbon composite ablation in rocket nozzles. Compos. Sci. Technol. **70**, 1303–1311 (2010)
45. Warren, J.A., Boettinger, W.J.: Prediction of dendritic growth and microsegregation patterns in a binary alloy using the phase-field method. Acta Metall. Mater. **43**, 689–703 (1995)
46. Whitaker, S.: The Method of Volume Averaging. Kluwer Academic, Dordrecht (1999)
47. Wood, J.R., Hewett, T.A.: Fluid convection and mass transfer in porous sandstones—a theoretical model. Geochim. Cosmochim. Acta **46**, 1907–1913 (1982)
48. Worster, M.G., Wettlaufer, J.S.: Natural convection, solute trapping, and channel formation during solidification of saltwater. J. Phys. Chem. B **101**, 6132–6136 (1997)
49. Xu, Z., Meakin, P.: Phase-field modeling of solute precipitation and dissolution. J. Chem. Phys. **129**, 014705 (2008)
50. Xu, Z., Meakin, P., Tartakovsky, A.M.: Diffuse-interface model for smoothed particle hydrodynamics. Phys. Rev. E **79**, 036702 (2009)
51. Yu, D., Ladd, A.J.C.: A numerical simulation method for dissolution in porous and fractured media. J. Comput. Phys. **229**, 6450–6465 (2010)
52. Zhao, C., Hobbs, B.E., Ord, A.: Fundamentals of Computational Geoscience: Numerical Methods and Algorithms. Springer, Berlin (2009)
53. Zhao, C., Hobbs, B.E., Ord, A.: Theoretical analyses of non-aqueous phase liquid dissolution-induced instability in two-dimensional fluid-saturated porous media. Int. J. Numer. Anal. Methods Geomech. **34**, 1767–1796 (2010)